Theoretical Development of Hybrid Simulation Applied to Plate Structures

Ahmed A. Bakhaty

Khalid M. Mosalam

Sanjay Govindjee

Department of Civil and Environmental Engineering
University of California, Berkeley

PEER Report 2014-02
Pacific Earthquake Engineering Research Center
Headquarters at the University of California, Berkeley

January 2014

Abstract

Hybrid simulation is a popular testing method for the experimental assessment of structural systems. The primary notion is to test only part of the system physically while simultaneously simulating the rest of the system via computer. While the basic idea is simple to understand, there is surprisingly little theoretical work targeted towards understanding the behavior of the concept and in particular its theoretical limitations. Although much attention has been devoted to reducing perceived error, little is actually known about what the reduction targets should be. In this report an initial investigation of the theoretical limitations of hybrid testing is presented in the context of a simple canonical setting: the Kirchhoff-Love plate bending dynamic problem. The physical system is mathematically separated into two pieces whose motions are exactly integrated analytically in closed-form. At the splitting interface, theoretical models associated with tracking and phase error of the boundary motions and forces are introduced. A parametric study is then performed to assess the resulting dependency of the error in the system response in terms of the interface models. Errors are represented in terms of a variety of norms, including L_2 norms, as well as a collection of semi-norms representing a variety of physically relevant resultant force-like quantities.

It is demonstrated that such systems are generally viable only below the first fundamental frequency of the system. At and above the fundamental frequency of the system, there are significant and unpredictable errors. Furthermore, it is shown that there is a tendency to accumulate global errors at the slightest introduction of any interface matching error, but that these errors become insensitive to further increase in mismatch. Finally, it is found that the different substructures are subject to excitation at their independent natural frequencies in addition to the natural frequencies of the hybrid system. Thus, in general, one needs to check both the natural frequencies of the whole as well as sub-systems in system design.

Acknowledgments

The project is made possible by the financial support of the National Science Foundation for the project "EAGER: Next Generation Hybrid Simulation - Evaluation and Theory" (Award Number: CMMI-1153665).

Any opinions, findings, and conclusions or recommendations expressed in this material are those of the author and do not necessarily reflect those of the National Science Foundation.

Contents

List of Figures

List of Notation

$\mathcal{B}$ Arbitrary physical body

$\mathcal{C}$ Computational substructure

$\mathcal{P}$ Physical substructure

$\square_c$ Quantity in $\mathcal{C}$-domain

$\square_p$ Quantity in $\mathcal{P}$-domain

$\bar{\square}$ Non-dimensional quantity (typically)

$\hat{\square}$ Quantity in hybrid domain

a Plate width (parallel to separation axis)

$A_{\bullet m} - L_{\bullet m}$ Fourier coefficients where $\bullet$ is for $\mathcal{B}$, $\mathcal{C}$, or $\mathcal{P}$

b Plate length (orthogonal to separation axis)

b_p Plate length in $\mathcal{P}$

b_c Plate length in $\mathcal{C}$

D Plate flexural rigidity

E Elastic (Young's) modulus

e Base of the natural logarithm

$||e_M||$ L_2 bending moment error norm

$||e_V||$ L_2 shear error norm

$||e_w||$ L_2 displacement error norm

$||e_\theta||$ L_2 rotation error norm

f_M Introduced error in bending moments

f_V Introduced error in shears

f_w Introduced error in displacements

f_θ	Introduced error in rotations
$\mathbf{g}$	Vector of boundary functions
g^w	Boundary function of displacement
g^θ	Boundary function of rotation
h	Thickness of plate
i	Imaginary unit ($\sqrt{-1}$)
m	Index of Fourier series
$\bar{M}$	Magnitude of applied harmonic bending moment
M_y	Bending moment per unit length about y-axis
M_{xy}	Twisting moment per unit length of edge with unit normal parallel to x-axis
V_y	Shear per unit length along edge with unit normal parallel to y-axis
t	Time
w	Out-of-plane displacement of plate
x	Cartesian coordinate (parallel to separation axis)
y	Cartesian coordinate (orthogonal to separation axis)
z	Cartesian coordinate (orthogonal to plane of plate)
α	Constant $m\pi/a$
β	Constant $\sqrt[4]{\frac{\rho h \omega^2}{D}}$
δ_k	Phase of k$^{\text{th}}$ gap
η	Normalized coordinate (orthogonal to separation axis)
γ	Real part of the positive roots of characteristic polynomial of ODE
Γ_m	Fourier coefficients of boundary functions
$\bar{\mu}$	Applied edge bending moment ratio $\frac{\bar{M}b}{D}$
ν	Poisson's ratio
Ω	Non-dimensional driving frequency
ω	Driving frequency of harmonic excitation
$\bar{\omega}_{mn}$	Natural frequency of plate

$\Omega_\bullet$	Domain of $\bullet$, where $\bullet$ is $\mathcal{B}$, $\mathcal{C}$, or $\mathcal{P}$
$\partial\Omega_\bullet$	Boundary of $\bullet$, where $\bullet$ is $\mathcal{B}$, $\mathcal{C}$, or $\mathcal{P}$
ψ	Non-dimensional out-of-plane displacement (w)
ρ	Mass density
θ	Rotation
ε_k	Magnitude of k^{th} gap
ξ	Normalized coordinate (parallel to separation axis)

1. Introduction

1.1 Motivation

Simulation and testing are critical aspects of engineering for the assessment, design, and production of efficient, economical, and safe structures, vehicles, engineering products, and other physical entities that play a fundamental role in modern society. The need to accurately and reliably simulate and predict the behavior of these entities is an ongoing challenge that has sparked a wide spectrum of interdisciplinary research, with the aim of developing robust, practical, and cost-efficient techniques and tools to achieve this goal. With the recent unprecedented growth in computational capability, numerical simulation has become the most widespread tool to solve the mathematical equations governing some of the behavior observed in the physical world. But these mathematical descriptions include inherent assumptions that often leave their results in disagreement with the actual response observed. Furthermore, there is not always a basis on which to validate these results, and the existence of finite precision in computing can lead to unreliable results. Thus experimental testing, the oldest and most fundamental technique of basic research, remains a necessary component of most, if not all, of engineering and science research today. However, like numerical modeling, experimentation faces many hindering challenges such as limitations due to cost, size, availability of resources, and reliable data acquisition.

Hybrid simulation, formerly known as pseudodynamic testing, has come forward as an analytical technique that serves to overcome the limitations of numerical simulation and experimental testing by combining the two: the components of a particular system that are difficult to accurately model mathematically are tested in the laboratory, while the remainder of the system that may be too large or costly to test is simulated numerically. As opposed to conventional testing, the specimen in the laboratory communicates with a computational model to receive commands and send feedback of its response. Unfortunately, hybrid simulation faces its own set of unique and inherent challenges, which leaves room for vigorous research to establish the technique as widespread as numerical simulation and experimental testing, not the least of which is the need for a well-defined theory. In the nearly forty years since its inception in the form of "on-line testing" [Takanashi et al. 1975], there has not been significant effort to define hybrid simulation in a theoretical framework. Specifically, the following question should be asked: Is hybrid simulation guaranteed to provide results representative of the actual behavior of what is being simulated?

One of the primary challenges of hybrid simulation is the impact of experimental, numerical, and control errors on the results [Mosqueda 2003]. These errors have been thoroughly studied in the context of pseudodynamic testing; typically, problem-driven mitigation strategies have been proposed that may not hold in general [Shing and Mahin 1983; Thewalt and Mahin 1987]. For instance, the errors due to control become more significant in real-time simulations where the time lag of the response of the servo-hydraulic system is critical [Conte and Trombetti 2000; Horiuchi et al. 1999]. This, there is an obvious need to develop a solid theoretical framework that will assess the effectiveness of hybrid testing while providing bounds on the errors in an effort to shift the focus of research to increased development of hybrid simulation techniques and applications as opposed to problem-driven studies of errors with solutions of limited scope.

The primary focus of hybrid simulation has traditionally been in the prediction and simulation of the response of structures (buildings, bridges, dams, tunnels, etc.) subjected to seismic excitation [Elkhoraibi and Mosalam 2007; Igarashi et al. 1993; Takanashi and Nakashima 1987]. The importance and merit of this goal continues to be a driving factor for the continued development of hybrid simulation because structures are in general far too large and costly to experimentally test, and hybrid simulation provides a cost-efficient and effective solution. Furthermore, the guaranteed performance and safety of critical facilities such as hospitals or power generation and distributions systems [Mosalam et al. 2012b] in the face of disasters (including earthquakes, hurricanes, blasts, and fire) is a necessary objective of society, notwithstanding the guaranteed safety of the inhabitants in all structures. However, it is important to note that the concept of hybrid simulation can be applied to other disciplines as well as to structures subjected to forces other than earthquakes. This has become increasingly important in light of recent events such as hurricanes and terrorist attacks that have rendered many structures, facilities, and vehicles in a state of great disrepair or inoperability. The problem-specific solutions proposed in previous and ongoing research in general may not hold in other applications, and a theoretical evaluation is necessary to validate the robustness of the technique across disciplines, as well as in the context of civil and earthquake engineering.

1.2 Background

Hybrid simulation has built on the early concept of pseudodynamic testing by making it possible to perform real-time and/or geographically-distributed simulations with more advanced control and communication methods, and including computational substructures of varying sizes [Dermitzakis and Mahin 1985]. Traditionally, the computational substructure is a finite element model, which communicates with the laboratory set-up via some sort of middleware [Schellenberg 2008]. A prime example of a general-use middleware software for hybrid simulation is the Open-source Framework for Experimental Setup and Control (OpenFresco) [OpenFresco 2013].

For the object to be simulated, governing equations (in a continuum or discrete formulation) are to be solved. The object is separated into computational and physical substructures, where the physical substructure provides the necessary component response to the driving (command) computational substructure via the measured laboratory response (feedback). In the example shown in Figure 1.1, a framed multistory, multibay building is subjected to an earthquake ground motion with a discrete finite element solution to the equations of motion computed in the numerical substructure. One of the elements, a column, exists in the laboratory and provides a stiffness and measured force feedback to the computational model in response to imposed displacement commands sent from the computational model to the actuators in the laboratory.

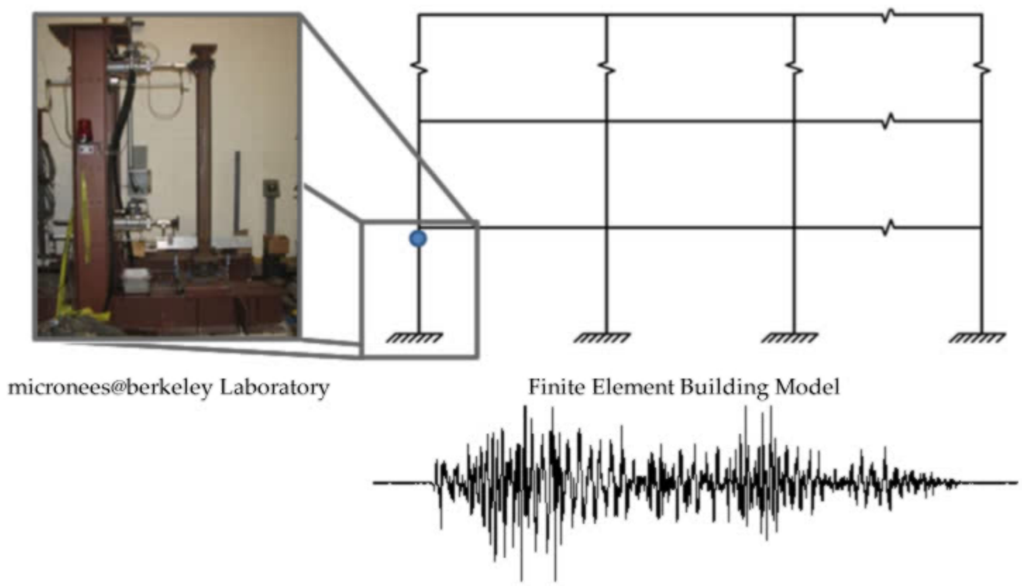

Figure 1.1: Schematic representation of hybrid simulation in seismic applications.

1.3 Problem Definition

The goal of this report is to present an initial investigation of the theoretical limitations of hybrid testing in the context of simple canonical settings. Starting with classical problems, corresponding "hybrid" problems can be formulated mathematically by arbitrarily separating the domain. The respective motions are then exactly integrated analytically in a closed-form while introducing a constraint at the interface of the two domains to capture the motion of the single full body. Theoretical models associated with the tracking and phase error of the boundary motions are introduced at the interface to simulate the effect of the incompatibility between the laboratory set-up and the numerical model. An example of an incompatibility is a time delay that results from the finite time it takes for an actuator to impose a displacement on the test specimen, measure the force feedback, and communicate it back to the numerical model [Horiuchi et al. 1999]. Note that this is not necessarily the most significant source of error present in hybrid testing, but it is inherent in and characteristic of hybrid simulation and is thus a focus of this study.

Some classical problems that could be studied are a one-dimensional rod subjected to dynamic axial loading, a one-dimensional beam subjected to dynamic bending [Govindjee 2012], and a two-dimensional plate subject to a dynamic bending. The plate is the focus of this report. The reader is referred to the work of Drazin for the bar and the beam [Drazin

2013]. The problem is separated mathematically, and a parametric error analysis is performed with respect to the "perfect" classical solution. The results presented herein are not intended to provide an exhaustive theory for hybrid simulation, but to introduce a theoretical investigation to be developed in continued endeavors.

With the emphasis of hybrid simulation to date being on skeletal structures that are dominated by flexural response, the beam is an appropriate starting point. The plate, however, plays a key role in structural engineering in the form of floor slabs and out-of-plane behavior of shear walls. These structural components tend to be large and very difficult to test due to complex boundary conditions and interaction with the rest of the structural system: this makes them ideal for hybrid testing. Moreover, outside the field of civil engineering, plates and shells comprise many critical components of vehicles, machinery, micro-electrical mechanical devices, and countless other objects that play an important role in modern society. With few hybrid simulation efforts being dedicated to these continuum elements, it becomes important to study them as part of the development of the next generation hybrid simulation methods.

1.4 Report Layout

Chapter 2 presents the theoretical formulation of hybrid simulation. First, the concept is introduced abstractly with a demonstration of the incompatibility of the substructures in a hybrid test. The Kirchhoff-Love dynamic plate bending problem is then formulated, and the hybrid concepts are applied. Chapter 3 introduces a method for studying the errors due to these incompatibilities relative to the true solution. A detailed study of these errors over a range of varying conditions is presented. Observations are noted, and their significance, limitations, and implications are discussed. Chapter 4 summarizes these findings and outlines the continued study and development of the theoretical framework of hybrid simulation. Appendix A through C present some mathematical details discussed in Chapter 2. Finally, Appendix D summarizes an experimental program carried out as part of an earlier stage of the project on the investigation of hybrid simulation with numerically intensive computational substructures. The results of this study are corroborated with the findings of the theoretical investigation in Chapter 3.

2. Theoretical Development of Hybrid Simulation

2.1 Introduction

The concept of hybrid simulation can be considered as a substructuring type analysis in which the domain is separated into various substructures that are analyzed or tested independently but accounts for interface conditions to render the response equivalent to that of a single global system [Dermitzakis and Mahin 1985]. Typically, there is a substructure intended for the laboratory or the "physical" substructure and a substructure intended for numerical analysis or the "computational" substructure. In general, hybrid simulation can involve any number of substructures, each being physical or computational with the possibility of being either all physical and all computational. These substructures may be geographically distributed [Campbell and Stojadinovic 1998] and may utilize different computational drivers for each computational substructure, as is possible with OpenFresco [Schellenberg 2008].

For simplicity, the theoretical treatment herein will involve only two separate domains, both of which have closed-form analytical solutions with the only error in the system coming from the imposed error at the interface and errors arising from finite machine precision in the evaluation of these solutions. The choice of separation is arbitrary in location; but at the risk of losing some generality, the orientation is selected to guarantee a well-behaving, closed-form mathematical expression. To avoid confusion, imposed error at the interface will generally be referred to as the "gap," while the overall error of the hybrid formulation relative to the analytical solutions will be referred to as the "error."

2.2 General Picture

Consider an arbitrary body $\mathcal{B}$ (Figure 2.1), with governing dynamic equation and boundary conditions given by Equation (2.1):

$$F[\mathbf{u}(\mathbf{r},t)] = \mathbf{0} \qquad \mathbf{r} \in \quad \Omega_{\mathcal{B}}, \tag{2.1a}$$

$$\mathbf{u}(\mathbf{r},t) = \bar{\mathbf{u}} \qquad \mathbf{r} \in \quad \partial\Omega_{\mathcal{B}}, \tag{2.1b}$$

where $\mathbf{u}$ is a characteristic quantity (e.g., displacements, velocities, accelerations, etc.), $\bar{\mathbf{u}}$ is an imposed value of that quantity on the boundary, $\mathbf{r}$ is the position in space, and t is the position in time.

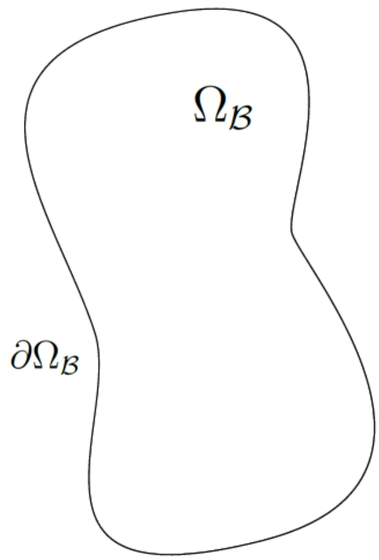

Figure 2.1: Arbitrary physical body.

$\mathcal{B}$ is now split into two subdomains, $\mathcal{P}$ and $\mathcal{C}$, as seen in Figure 2.2, referred to as the $\mathcal{P}$-domain and $\mathcal{C}$-domain, respectively. Each domain is governed by the same equations but subjected to separate boundary conditions and local coordinate systems:

$$F[\hat{\mathbf{u}}_p(\mathbf{r}_p, t)] = \mathbf{0} \qquad \mathbf{r}_p \in \Omega_{\mathcal{P}}, \tag{2.2a}$$
$$\hat{\mathbf{u}}_p(\mathbf{r}_p, t) = \bar{\mathbf{u}}_p \qquad \mathbf{r}_p \in \partial\Omega_{\mathcal{P}}, \tag{2.2b}$$
$$F[\hat{\mathbf{u}}_c(\mathbf{r}_c, t)] = \mathbf{0} \qquad \mathbf{r}_c \in \Omega_{\mathcal{C}}, \tag{2.2c}$$
$$\hat{\mathbf{u}}_c(\mathbf{r}_c, t) = \bar{\mathbf{u}}_c \qquad \mathbf{r}_c \in \partial\Omega_{\mathcal{C}}. \tag{2.2d}$$

The following relations hold:

$$\hat{\Omega}_{\mathcal{B}} = \Omega_{\mathcal{P}} \cup \Omega_{\mathcal{C}}, \tag{2.3a}$$
$$\hat{\mathbf{u}} = \hat{\mathbf{u}}_p \cup \hat{\mathbf{u}}_c, \tag{2.3b}$$
$$\partial\Omega_{\mathcal{B}} = \partial\Omega_{\mathcal{P}} \cup \partial\Omega_{\mathcal{C}} - \partial\Omega_{\mathcal{P}} \cap \partial\Omega_{\mathcal{C}}, \tag{2.3c}$$

where $\hat{\Omega}_{\mathcal{B}}$ is introduced as the corresponding hybrid domain of $\Omega_{\mathcal{B}}$, and $\hat{\mathbf{u}}$ is the corresponding unified response in the joint hybrid domain. From Equation (2.3c) and Figure 2.2, it is clear there is an interface between $\mathcal{P}$ and $\mathcal{C}$, $\partial\Omega_{\mathcal{P}} \cap \partial\Omega_{\mathcal{C}} \in \hat{\Omega}_{\mathcal{B}}$, for which additional boundary conditions on the split domain must be furnished to satisfy Equation (2.2). These boundary conditions are

$$\hat{\mathbf{u}}_p(\mathbf{r}_p, t) = \mathbf{g}_p(\mathbf{r}_p, t) \qquad \mathbf{r}_p \in \partial\Omega_{\mathcal{P}} \cap \partial\Omega_{\mathcal{C}}, \tag{2.4a}$$
$$\hat{\mathbf{u}}_c(\mathbf{r}_c, t) = \mathbf{g}_c(\mathbf{r}_c, t) \qquad \mathbf{r}_c \in \partial\Omega_{\mathcal{P}} \cap \partial\Omega_{\mathcal{C}}, \tag{2.4b}$$

where $\mathbf{g}_p$ and $\mathbf{g}_c$ are "boundary functions" introduced to furnish the additional boundary conditions needed on the interface of the $\mathcal{P}$-domain and $\mathcal{C}$-domain, respectively. For the hybrid system, $\mathbf{g}_p$ and $\mathbf{g}_c$ are not independent but are related to each either via a constraint.

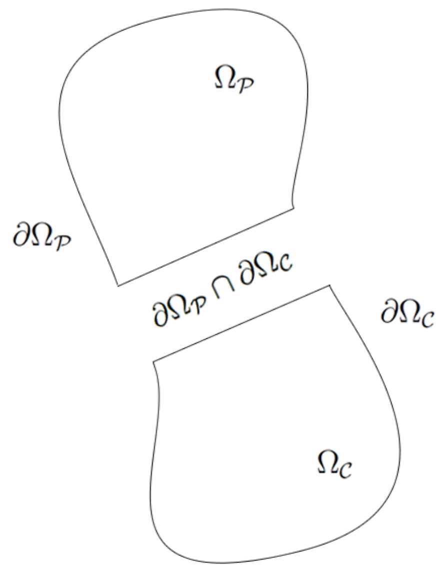

Figure 2.2: Separated "hybrid" domain.

By forcing them to be unequal, a "gap" is formed between the two domains. To achieve equivalence of the joint $\mathcal{P}$-domain and $\mathcal{C}$-domain to $\mathcal{B}$, the boundary functions are constrained to match:

$$\mathbf{g}_p = \mathbf{g}_c, \tag{2.5a}$$

$$\Longrightarrow \hat{\Omega}_{\mathcal{B}} = \Omega_{\mathcal{B}}. \tag{2.5b}$$

In the context of hybrid simulation, the boundary functions are forced to be incompatible by introducing an error. In general, the condition on the boundary functions is expressed as

$$G[\mathbf{g}_p, \mathbf{g}_c] = \mathbf{0}, \tag{2.6}$$

where G is a constraint functional. In hybrid simulation, the computational substructure is subjected to some excitation. In this study the physical substructure's response is determined by the measured response of the testing due to the computed interface excitation. Following this methodology, the $\mathcal{C}$-domain will be subjected to an excitation, which then enters the $\mathcal{P}$-domain via the boundary functions through the constraint given by Equation (2.6). In the context of a structural mechanics problem, the boundary functions are selected to assume characteristic physical quantities such as displacements, rotations, bending moments, and shears. The constraints given by Equation (2.6) then represent a mismatch in these quantities across the interface. A key example of this mismatch is a time delay between the response quantities of the computational and physical substructures due to the finite time required to move the actuators in the laboratory [Horiuchi et al. 1999]. A simple expression for this mismatch is of the k^{th} boundary function is

$$g_p^k = g_c^k(1 + \varepsilon_k)e^{-i\Omega d_k} \tag{2.7}$$

where $i = \sqrt{-1}$ is the imaginary unit, ε_k controls the magnitude of the error, δ_k controls the phase of the error, and Ω is a characteristic frequency of the system. This relation can be modified to include the effect of frequency dependence on the error. Physically speaking, a controller will have more difficulty keeping up while operating at higher frequencies and larger error is observed when compared to lower frequencies [Conte and Trombetti 2000]. Making use of the generalized logistic function [Richards 1959], a simple frequency dependent error gap model, as shown in Figure 2.3, may be expressed as

$$\varepsilon_k(\omega) = \frac{\varepsilon_0}{(1 + e^{(\omega_0 - \omega)})^2}, \tag{2.8}$$

where ε_0 is a maximum error magnitude, and ω_0 is the frequency of maximum growth rate.

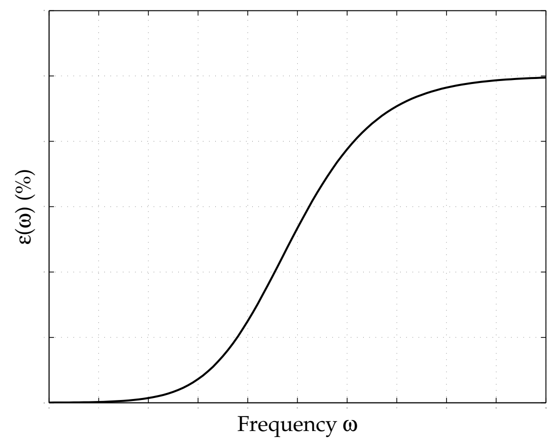

Figure 2.3: Example of the frequency-dependent error model.

2.3 Kirchhoff-Love "Thin" Plate

Consider a simply supported homogeneous, isotropic Kirchhoff-Love “thin” plate of uniform thickness h, mass density ρ, and elastic modulus E, subjected to a harmonic edge moment $M(x, b, t) = \bar{M}e^{i\omega t}$, as shown in Figure 2.4.

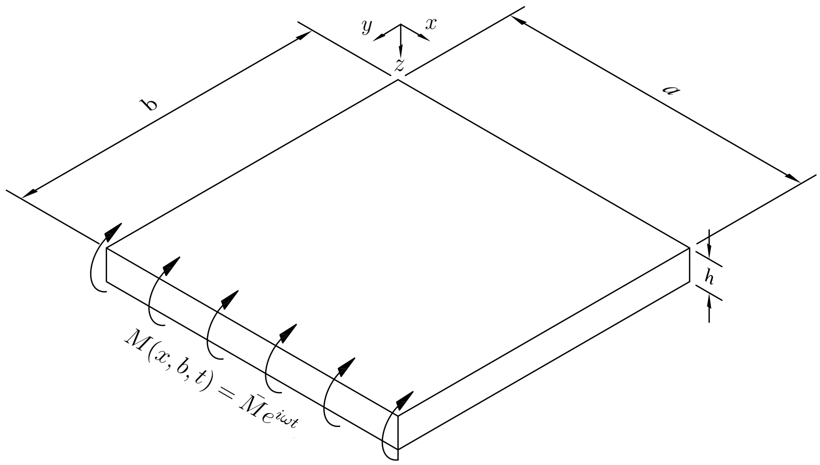

Figure 2.4: Simply supported homogeneous Kirchhoff plate with harmonic edge moment.

The governing equation of motion for the transverse displacements w is given by [Graff 1975]

$$D\nabla^4 w + \rho h \frac{\partial^2 w}{\partial t^2} = 0, \tag{2.9}$$

where $\nabla^4 = \frac{\partial^4}{\partial x^4} + 2\frac{\partial^4}{\partial x \partial y} + \frac{\partial^4}{\partial y^4}$ is the biharmonic operator. The definitions of the various plate terms used throughout can be found in Appendix A. The flexural rigidity D is defined as

$$D = \frac{Eh^3}{12(1-\nu^2)}. \tag{2.10}$$

The boundary conditions for this system are

$$w(0, y, t) = w(a, y, t) = 0, \tag{2.11a}$$

$$w(x, 0, t) = w(x, b, t) = 0, \tag{2.11b}$$

$$\left.\frac{\partial^2 w}{\partial x^2}\right|_{x=0} = \left.\frac{\partial^2 w}{\partial x^2}\right|_{x=a} = 0, \tag{2.11c}$$

$$\left.\frac{\partial^2 w}{\partial y^2}\right|_{y=0} = 0, \tag{2.11d}$$

$$-D\left.\frac{\partial^2 w}{\partial y^2}\right|_{y=b} = \bar{M}e^{i\omega t}. \tag{2.11e}$$

Lévy has proposed a solution where a Fourier sine series is assumed in one direction, with the coefficients being functions of the orthogonal direction [Timoshenko 1959]:

$$
\begin{aligned}
w(x,y,t) &= W(x,y)T(t), && \text{(2.12a)}\\
T(t) &= e^{i\omega t}, && \text{(2.12b)}\\
W(x,y) &= \sum_{m=1}^{\infty} Y_m(y)\sin(\alpha_m x), && \text{(2.12c)}\\
\alpha_m &= \frac{m\pi}{a}. && \text{(2.12d)}
\end{aligned}
$$

The primary advantage of this method is a significantly more rapid convergence than the traditional double sine series [Taylor and Govindjee 2004]. Furthermore, the plate can be separated along the direction of the sine series, providing a convenient formulation of the solution orthogonal to the separation. One major drawback noted by Taylor and Govindjee [Taylor and Govindjee 2004] is the presence of the hyperbolic terms may lead to some numerical instability, addressed in Section 2.5.

Substituting Equation (2.12a) into Equation (2.9) leads to the following fourth order ODE

$$
Y_m'''' - 2\alpha_m^2 Y_m'' - (\beta^4 - \alpha_m^4)Y_m = 0, \tag{2.13}
$$

where

$$
\beta^4 = \frac{\rho h \omega^2}{D}. \tag{2.14a}
$$

The roots of the characteristic polynomial of Equation (2.13) are

$$
\begin{aligned}
r_1, r_2 &= \pm\sqrt{\beta^2 + \alpha_m^2}, && \text{(2.15a)}\\
r_3, r_4 &= \pm\sqrt{\beta^2 - \alpha_m^2}. && \text{(2.15b)}
\end{aligned}
$$

From Equation (2.17b), it is apparent that the characteristic equation may have complex or repeated roots. Therefore, the form of the solution will in general vary for increasing terms in the series as well as for different driving frequencies and geometry [Leissa 1969]. The solution to Equation (2.9) is given by [Gorman and Sharma 1976]

$$
\begin{aligned}
w(x,y,t) = &\sum_{m=1,3,\ldots}^{m_c} \sin(\alpha_m x)[A_m\cosh(\gamma_1 y) + B_m\sinh(\gamma_1 y)\\
&\qquad + C_m\cos(\gamma_2 y) + D_m\sin(\gamma_2 y)]e^{i\omega t}\\
+ &\sum_{m=m_c+1,m_c+3,\ldots}^{m_r} \sin(\alpha_m x)[E_m\cosh(\gamma_1 y) + F_m\sinh(\gamma_1 y)\\
&\qquad + G_m y\cosh(\gamma_1 y) + H_m y\sinh(\gamma_1 y)]e^{i\omega t}\\
+ &\sum_{m=m_r+1,m_r+3,\ldots}^{\infty} \sin(\alpha_m x)[I_m\cosh(\gamma_1 y) + J_m\sinh(\gamma_1 y)\\
&\qquad + K_m\cosh(-\gamma_2 y) + L_m\sinh(-\gamma_2 y)]e^{i\omega t}.
\end{aligned}
\tag{2.16}
$$

where $\alpha_m^4 > \beta^4$ for $m \leq m_c$, $\alpha_m^4 = \beta^4$ for $m_c < m \leq m_r$, and $\alpha_m^4 > \beta^4$ for $m > m_r$ and

$$\gamma_1 = \sqrt{\beta^2 + \alpha_m^2}, \tag{2.17a}$$

$$\gamma_2 = \sqrt{|\beta^2 - \alpha_m^2|}. \tag{2.17b}$$

The selection of the Fourier sine series in x automatically satisfies Equation (2.11a). The coefficients A_m through L_m are determined by imposing the remaining boundary conditions. In order to impose Equation (2.11e), a Fourier expansion is performed:

$$-D\frac{\partial^2 w}{\partial y^2}\bigg|_{y=b} = \bar{M}e^{i\omega t} = \frac{4\bar{M}}{\pi}\sum_{m=1,3,\ldots}^{\infty}\frac{1}{m}\sin(\alpha_m x)e^{i\omega t}. \tag{2.18}$$

By imposing the boundary conditions on Equation (2.16), the following solution is determined:

$$\begin{aligned} w(x,y,t) = &\sum_{m=1,3,\ldots}^{m_c} w_0 \sin(\alpha_m x)\left(\frac{\sin(\gamma_2 y)}{\sin(\gamma_2 b)} - \frac{\sinh(\gamma_1 y)}{\sinh(\gamma_1 b)}\right)e^{i\omega t} \\ &+ \sum_{m=m_c+1,m_c+3,\ldots}^{m_r} w_0' \sin(\alpha_m x)\left(b\coth(\gamma_1 b)\frac{\sinh(\gamma_1 y)}{\sinh(\gamma_1 b)} - y\frac{\cosh(\gamma_1 y)}{\sinh(\gamma_1 b)}\right)e^{i\omega t} \\ &+ \sum_{m=m_r+1,m_r+3,\ldots}^{\infty} w_0^* \sin(\alpha_m x)\left(\frac{\sinh(-\gamma_2 y)}{\sinh(-\gamma_2 b)} - \frac{\sinh(\gamma_1 y)}{\sinh(\gamma_1 b)}\right)e^{i\omega t}, \end{aligned} \tag{2.19}$$

where

$$w_0 = \frac{4\bar{M}}{m\pi D(\gamma_1^2 + \gamma_2^2)}, \tag{2.20a}$$

$$w_0^* = \frac{4\bar{M}}{m\pi D(\gamma_1^2 - \gamma_2^2)}, \tag{2.20b}$$

$$w_0' = \frac{2\bar{M}}{m\pi D\gamma_1}. \tag{2.20c}$$

The natural frequencies and mode shapes of the simply supported plates were initially solved by Navier [Szilard 2004] and Gorman and Sharma [Gorman and Sharma 1976] have shown it to be consistent with the Lévy solution.

$$\bar{\omega}_{mn} = \pi^2\sqrt{\tfrac{D}{\rho h}}\left(\tfrac{m^2}{a^2} + \tfrac{n^2}{b^2}\right), \qquad \text{for } m,n \in \mathbb{Z}^+ \tag{2.21a}$$

$$w_{mn}(x,y) = \sin(\tfrac{m\pi x}{a})\sin(\tfrac{n\pi y}{b}) \quad . \tag{2.21b}$$

Figure 2.5 shows the response of a square plate subjected to a harmonic edge moment driven at a forcing frequency ω near the natural frequencies $\bar{\omega}_{mn}$ of the plate. The plots were generated with the Matlab® programming language software package [MATLAB 2013].

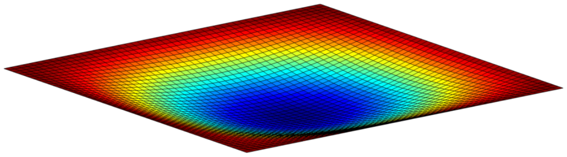
(a) m=1, n=1

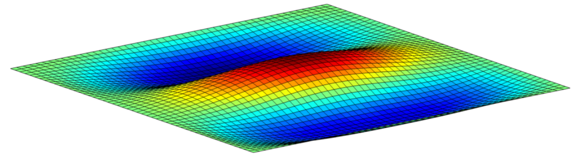
(b) m=1, n=3

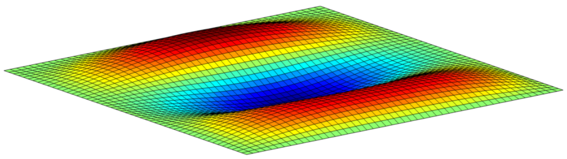
(c) m=3, n=1

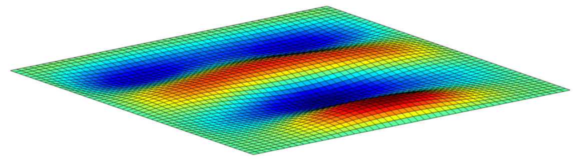
(d) m=3, n=3

Figure 2.5: Plate response at driving frequency near the natural frequencies.

2.4 Hybrid Plate

Consider the plate from Section 2.3 separated into the $\mathcal{P}$-domain and $\mathcal{C}$-domain as depicted in Figure 2.6, with boundary functions defined at the interface. Here g_p^w and g_c^w are selected as displacements and g_p^θ and g_c^θ are rotations about the x-axis.

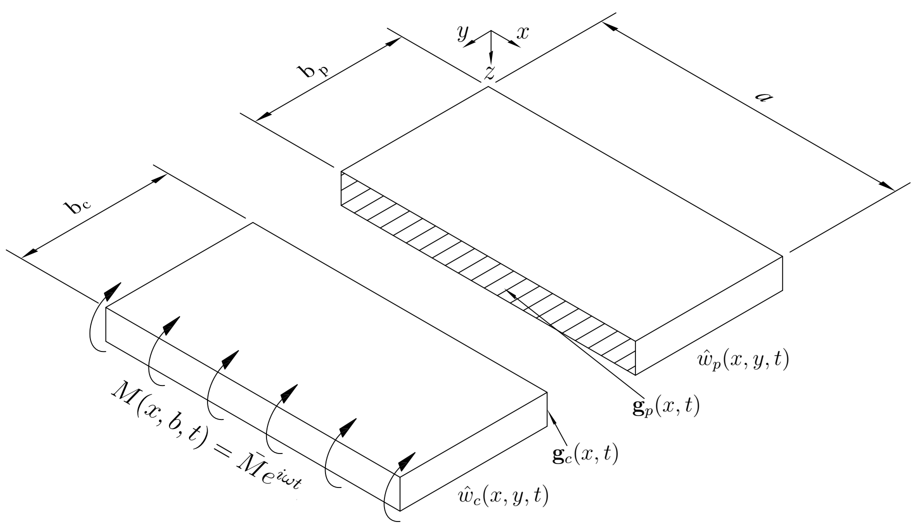

Figure 2.6: Hybrid thin plate with "physical" and "computational" substructures.

The full plate is then the union of the individual solutions for each domain as introduced in Equation (2.3)

$$\hat{w}(x,y,t) = \begin{cases} \hat{w}_p(x,y,t) & \text{for } y \in [0,b_p] \\ \hat{w}_c(x,y,t) & \text{for } y' \in [0,b_c]. \end{cases} \tag{2.22}$$

The coordinate transformation $y' = b - y$ is introduced for convenience and it holds that $b_p + b_c = b$. The solution form for each domain is assumed to be similar to Equation (2.12a):

$$\hat{w}_p(x,y,t) = \hat{W}_p(x,y)T_p(t), \tag{2.23a}$$

$$T_p(t) = e^{i\omega_p t}, \tag{2.23b}$$

$$\hat{w}_c(x,y',t) = \hat{W}_c(x,y')T_c(t), \tag{2.23c}$$

$$T_c(t) = e^{i\omega_c t}. \tag{2.23d}$$

Applying Lévy's method to each domain, the solutions are expressed similar to Equation (2.16).

For the $\mathcal{P}$-domain or $x \in [0,a]$ and $y \in [0,b_p]$

$$\begin{aligned} \hat{w}_p(x,y,t) = &\sum_{m=1,3,\ldots}^{m_c} \sin(\alpha_{pm}x)[A_{pm}\cosh(\gamma_{p1}y) + B_{pm}\sinh(\gamma_{p1}y) \\ &\qquad + C_{pm}\cos(\gamma_{p2}y) + D_{pm}\sin(\gamma_{p2}y)]e^{i\omega_p t} \\ + &\sum_{m=m_c+1,m_c+3,\ldots}^{m_r} \sin(\alpha_{pm}x)[E_{pm}\cosh(\gamma_{p1}y) + F_{pm}\sinh(\gamma_{p1}y) \\ &\qquad + G_{pm}y\cosh(\gamma_{p1}y) + H_{pm}y\sinh(\gamma_{p1}y)]e^{i\omega_p t} \\ + &\sum_{m=m_r+1,m_r+3,\ldots}^{\infty} \sin(\alpha_{pm}x)[I_{pm}\cosh(\gamma_{p1}y) + J_{pm}\sinh(\gamma_{p1}y) \\ &\qquad + K_{pm}\cosh(-\gamma_{p2}y) + L_{pm}\sinh(-\gamma_{p2}y)]e^{i\omega_p t}. \end{aligned} \tag{2.24}$$

For the $\mathcal{C}$-domain or $x \in [0,a]$ and $y' \in [0,b_c]$

$$\begin{aligned} \hat{w}_c(x,y,t) = &\sum_{m=1,3,\ldots}^{m_c} \sin(\alpha_{cm}x)[A_{cm}\cosh(\gamma_{c1}y') + B_{cm}\sinh(\gamma_{c1}y') \\ &\qquad + C_{cm}\cos(\gamma_{c2}y') + D_{cm}\sin(\gamma_{c2}y')]e^{i\omega_c t} \\ + &\sum_{m=m_c+1,m_c+3,\ldots}^{m_r} \sin(\alpha_{cm}x)[E_{cm}\cosh(\gamma_{c1}y') + F_{cm}\sinh(\gamma_{c1}y') \\ &\qquad + G_{cm}y'\cosh(\gamma_{c1}y') + H_{cm}y'\sinh(\gamma_{c1}y')]e^{i\omega_c t} \\ + &\sum_{m=m_r+1,m_r+3,\ldots}^{\infty} \sin(\alpha_{cm}x)[I_{cm}\cosh(\gamma_{c1}y') + J_{cm}\sinh(\gamma_{c1}y') \\ &\qquad + K_{cm}\cosh(-\gamma_{c2}y') + L_{cm}\sinh(-\gamma_{c2}y')]e^{i\omega_c t}. \end{aligned} \tag{2.25}$$

It is assumed that the frequencies of the solutions, ω_p and ω_c, are continuous across the domains and comply with the driving frequency ω. This condition leads to

$$\omega_p = \omega_c = \omega, \tag{2.26a}$$
$$\alpha_{pm} = \alpha_{cm} = \alpha_m, \tag{2.26b}$$
$$\beta_p^4 = \beta_c^4 = \beta^4, \tag{2.26c}$$
$$\gamma_{p1} = \gamma_{c1} = \sqrt{\alpha_m^2 + \beta^2}, \tag{2.26d}$$
$$\gamma_{p2} = \gamma_{c2} = \sqrt{\alpha_m^2 - \beta^2}. \tag{2.26e}$$

In the spirit of substructuring analysis, each domain is considered separately and the results subsequently merged.

2.4.1 $\mathcal{P}$-Domain

The boundary conditions on the $\mathcal{P}$-domain are

$$\hat{w}_p(0,y,t) = \hat{w}_p(a,y,t) = 0, \tag{2.27a}$$
$$\left.\frac{\partial^2 \hat{w}_p}{\partial x^2}\right|_{x=0} = \left.\frac{\partial^2 \hat{w}_p}{\partial x^2}\right|_{x=a} = 0, \tag{2.27b}$$
$$\hat{w}_p(x,0,t) = 0, \tag{2.27c}$$
$$\left.\frac{\partial^2 \hat{w}_p}{\partial y^2}\right|_{y=0} = 0, \tag{2.27d}$$
$$\hat{w}_p(x,b_p,t) = g_p^w(x,t) = \sum_{m=1,3,\ldots}^{\infty} \Gamma_{pm}^w \sin(\alpha_{pm}x)e^{i\omega_p t}, \tag{2.27e}$$
$$\left.\frac{\partial \hat{w}_p}{\partial y}\right|_{y=b_p} = g_p^\theta(x,t) = \sum_{m=1,3,\ldots}^{\infty} \Gamma_{pm}^\theta \sin(\alpha_{pm}x)e^{i\omega_p t}. \tag{2.27f}$$

Because the boundary functions are selected as displacements and rotations at the interface $y = b_p$ along x, the Fourier expansions are assumed to be of the form given by Equations (2.27e) and (2.27f) to maintain consistency with the Lévy solution.

By substituting these boundary conditions into Equation (2.24), the coefficients A_{pm} through L_{pm} are determined:

$$A_{pm} = 0, \tag{2.28a}$$
$$B_{pm} = \frac{-\gamma_{p2}\cos(\gamma_{p2}b_p)\gamma_{p1} + \sin(\gamma_{p2}b_p)\Gamma_{pm}^\theta}{R_1}, \tag{2.28b}$$
$$C_{pm} = 0, \tag{2.28c}$$
$$D_{pm} = \frac{\gamma_{p1}\cosh(\gamma_{p1}b_p)\gamma_{p1} - \sinh(\gamma_{p1}b_p)\Gamma_{pm}^\theta}{R_1}, \tag{2.28d}$$
$$E_{pm} = 0, \tag{2.28e}$$

$$
\begin{aligned}
F_{pm} &= \frac{(\gamma_{p1} b_p \sinh(\gamma_{p1} b_p) + \cosh(\gamma_{p1} b_p))\gamma_{p1} - b_p \cosh(\gamma_{p1} b_p)\Gamma^{\theta}_{pm}}{R'_1}, && (2.28\text{f}) \\
G_{pm} &= \frac{-\gamma_{p1} \cosh(\gamma_{p1} b_p)\gamma_{p1} + \sinh(\gamma_{p1} b_p)\Gamma^{\theta}_{pm}}{R'_1}, && (2.28\text{g}) \\
H_{pm} &= 0, && (2.28\text{h}) \\
I_{pm} &= 0, && (2.28\text{i}) \\
J_{pm} &= \frac{-\gamma_{p2} \cosh(\gamma_{p2} b_p)\gamma_{p1} + \sinh(\gamma_{p2} b_p)\Gamma^{\theta}_{pm}}{R^*_1}, && (2.28\text{j}) \\
K_{pm} &= 0, && (2.28\text{k}) \\
L_{pm} &= \frac{\gamma_{p1} \cosh(\gamma_{p1} b_p)\gamma_{p1} - \sinh(\gamma_{p1} b_p)\Gamma^{\theta}_{pm}}{R^*_1}. && (2.28\text{l})
\end{aligned}
$$

where

$$
\begin{aligned}
R_1 &= \gamma_{p1} \cosh(\gamma_{p1} b_p) \sin(\gamma_{p2} b_p) - \gamma_{p2} \sinh(\gamma_{p1} b_p) \cos(\gamma_{p2} b_p), && (2.29\text{a}) \\
R^*_1 &= \gamma_{p1} \cosh(\gamma_{p1} b_p) \sinh(-\gamma_{p2}\ b_p) - \gamma_{p2} \sinh(\gamma_{p1} b_p) \cos(-\gamma_{p2} b_p), && (2.29\text{b}) \\
R'_1 &= \sinh(\gamma_{p1} b_p) \cosh(\gamma_{p1} b_p) - \gamma_{p1} b_p. && (2.29\text{c})
\end{aligned}
$$

Note again that the excitation enters the $\mathcal{P}$-domain through $g^w_p(x,t)$ and $g^\theta_p(x,t)$ at the interface by imposing a constraint on these functions with their counterparts in the $\mathcal{C}$-domain $g^w_c(x,t)$ and $g^\theta_c(x,t)$, respectively.

2.4.2 $\mathcal{C}$-Domain

Similar to the $\mathcal{P}$-domain, the boundary conditions for the $\mathcal{C}$-domain are

$$
\begin{aligned}
\hat{w}_c(0, y', t) = \hat{w}_c(a, y', t) &= 0, && (2.30\text{a}) \\
\left.\frac{\partial^2 \hat{w}_c}{\partial x^2}\right|_{x=0} = \left.\frac{\partial^2 \hat{w}_c}{\partial x^2}\right|_{x=a} &= 0, && (2.30\text{b}) \\
\hat{w}_c(x, 0, t) &= 0, && (2.30\text{c}) \\
\left.\frac{\partial^2 \hat{w}_c}{\partial y'^2}\right|_{y'=0} &= -\frac{4\bar{M}}{\pi D} \sum_{m=1,3,\ldots}^{\infty} \frac{1}{m} \sin(\alpha_{cm} x) e^{i\omega_c t}, && (2.30\text{d}) \\
\hat{w}_c(x, b_c, t) = g^w_c(x,t) &= \sum_{m=1,3,\ldots}^{\infty} \Gamma^w_{cm} \sin(\alpha_{cm} x) e^{i\omega_c t}, && (2.30\text{e}) \\
\left.\frac{\partial \hat{w}_c}{\partial y'}\right|_{y'=b_c} = g^\theta_c(x,t) &= \sum_{m=1,3,\ldots}^{\infty} \Gamma^\theta_{cm} \sin(\alpha_{cm} x) e^{i\omega_c t}. && (2.30\text{f})
\end{aligned}
$$

By substituting these boundary conditions into Equation (2.25), the coefficients A_{cm}

through L_{cm} can be determined:

$$A_{cm} = -w_0, \tag{2.31a}$$
$$B_{cm} = \frac{-\gamma_{c2}\cos(\gamma_{c2}b_c)\gamma_{c2} + \sin(\gamma_{c2}b_c)\Gamma^{\theta}_{cm} + w_0(\gamma_{c2} + P_1)}{R_2}, \tag{2.31b}$$
$$C_{cm} = w_0, \tag{2.31c}$$
$$D_{cm} = \frac{\gamma_{c1}\cosh(\gamma_{c1}b_c)\gamma_{c2} + \sinh(\gamma_{c1}b_c)\Gamma^{\theta}_{cm} + w_0(\gamma_{c1} - P_2)}{R_2}, \tag{2.31d}$$
$$E_{cm} = 0, \tag{2.31e}$$
$$F_{cm} = \frac{(\gamma_{c1}b_c\sinh(\gamma_{c1}b_c) + \cosh(\gamma_{c1}b_c))\gamma_{c2} - b_c\cosh(\gamma_{c1}b_c)\Gamma^{\theta}_{cm} - w_0'\gamma_{c1}b_c^2}{R_2'}, \tag{2.31f}$$
$$G_{cm} = \frac{-\gamma_{c1}\cosh(\gamma_{c1}b_c)\gamma_{c2} + \sinh(\gamma_{c1}b_c)\Gamma^{\theta}_{cm} + w_0'\sinh^2(\gamma_{c1}b_c)}{R_2'}, \tag{2.31g}$$
$$H_{cm} = -w_0', \tag{2.31h}$$
$$I_{cm} = -w_0^*, \tag{2.31i}$$
$$J_{cm} = \frac{-\gamma_{c2}\cosh(\gamma_{c2}'b_c)\gamma_{c2} + \sin(\gamma_{c2}'b_c)\Gamma^{\theta}_{cm} - w_0^*(\gamma_{c2}' + P_1^*)}{R_2^*}, \tag{2.31j}$$
$$K_{cm} = w_0^*, \tag{2.31k}$$
$$L_{cm} = \frac{\gamma_{c1}\cosh(\gamma_{c1}b_c)\gamma_{c2} + \sinh(\gamma_{c1}b_c)\Gamma^{\theta}_{cm} - w_0^*(\gamma_{c1} - P_2^*)}{R_2^*}. \tag{2.31l}$$

where

$$R_2 = \gamma_{c1}\cosh(\gamma_{c1}b_c)\sin(\gamma_{c2}b_c) - \gamma_{c2}\sinh(\gamma_{c1}b_c)\cos(\gamma_{c2}b_c), \tag{2.32a}$$
$$P_1 = \gamma_{c1}\sinh(\gamma_{c1}b_c)\sin(\gamma_{c2}b_c) - \gamma_{c2}\cosh(\gamma_{c1}b_c)\cos(\gamma_{c2}b_c), \tag{2.32b}$$
$$P_2 = \gamma_{c2}\sinh(\gamma_{c1}b_c)\sin(\gamma_{c2}b_c) + \gamma_{c1}\cosh(\gamma_{c1}b_c)\cos(\gamma_{c2}b_c), \tag{2.32c}$$
$$R_2' = \sinh(\gamma_{c1}b_c)\cosh(\gamma_{c1}b_c) - \gamma_{c1}b_c, \tag{2.32d}$$
$$R_2^* = \gamma_{c1}\cosh(\gamma_{c1}b_c)\sinh(-\gamma_{c2}b_c) + \gamma_{c2}\sinh(\gamma_{c1}b_c)\cosh(\gamma_{c2}b_c), \tag{2.32e}$$
$$P_1^* = \gamma_{c1}\sinh(\gamma_{c1}b_c)\sinh(-\gamma_{c2}b_c) + \gamma_{c2}\cosh(\gamma_{c1}b_c)\cosh(\gamma_{c2}b_c), \tag{2.32f}$$
$$P_2^* = -\gamma_{c2}\sinh(\gamma_{c1}b_c)\sinh(-\gamma_{c2}b_c) - \gamma_{c1}\cosh(\gamma_{c1}b_c)\cosh(\gamma_{c2}b_c). \tag{2.32g}$$

2.4.3 $\mathcal{P} \cup \mathcal{C}$ Joint Domain

Because the boundary functions are not explicitly defined, two more relations in addition to Equation (2.6) are required to determine properly the unique solutions $\hat{w}_p$ and $\hat{w}_c$. These are furnished by constraints on the bending moment and shear at the interface. Because the force quantities in a hybrid test will also have error associated with them, gaps of the form given by Equation (2.7) are imposed on the bending moment and shear.

$$g_p^w(x,t) - f_w g_c^w(x,t) = 0, \tag{2.33a}$$

$$g_p^\theta(x,t) - f_\theta g_c^\theta(x,t) = 0, \tag{2.33b}$$

$$\hat{M}_{py}(x,b_p,t) - f_M \hat{M}_{cy'}(x,b_c,t) = 0, \tag{2.33c}$$

$$\hat{V}_{py}(x,b_p,t) - f_V \hat{V}_{cy'}(x,b_c,t) = 0. \tag{2.33d}$$

Because the rotation, $\partial w/\partial y$, has been specified, the twisting moment is also necessarily specified (see Appendix A for the definition of the twisting moment), implying that an additional condition on the twisting moment is redundant.

2.5 Perfect Conditions

Naturally the first case to be considered is the absence of any inconsistencies between the two domains in which the results should be equivalent to those of Section 2.3. This is achieved with zero gap or $f_w = f_\theta = f_M = f_V = 1$. Accordingly, Equation (2.33) becomes

$$g_p^w(x,t) - g_c^w(x,t) = 0, \tag{2.34a}$$

$$g_p^\theta(x,t) - g_c^\theta(x,t) = 0, \tag{2.34b}$$

$$\hat{M}_{py}(x,b_p,t) - \hat{M}_{cy'}(x,b_c,t) = 0, \tag{2.34c}$$

$$\hat{V}_{py}(x,b_p,t) - \hat{V}_{cy'}(x,b_c,t) = 0. \tag{2.34d}$$

These relations can be expressed in terms of the Fourier coefficients Γ_m of the boundary functions while taking note that without the introduction of additional boundary functions, the bending moments and shears are functions of these coefficients. The terms below can be found in Appendix A.

$$\Gamma_{pm}^w = \Gamma_{cm}^w, \tag{2.35a}$$

$$\Gamma_{pm}^\theta = \Gamma_{cm}^\theta, \tag{2.35b}$$

$$\left[\nu\frac{\partial^2 \hat{w}_p}{\partial x^2} + \frac{\partial^2 \hat{w}_p}{\partial y^2}\right]_{y=b_p} = \left[\frac{\partial^2 \hat{w}_c}{\partial y'^2} + \nu\frac{\partial^2 \hat{w}_c}{\partial x^2}\right]_{y'=b_c}, \tag{2.35c}$$

$$\left[(1-2\nu)\frac{\partial^3 \hat{w}_p}{\partial x^2 \partial y} + \frac{\partial^3 \hat{w}_p}{\partial y^3}\right]_{y=b_p} = \left[\frac{\partial^3 \hat{w}_c}{\partial y'^3} + \frac{\partial^2 \hat{w}_c}{\partial x^2 \partial y'}(1-2\nu)\right]_{y'=b_c}. \tag{2.35d}$$

By imposing these relations on Equations (2.24) and (2.25), the following system of algebraic equations can be used to solved for the Fourier coefficients:

$$\begin{pmatrix} 1 & -1 & 0 & 0 \\ 0 & 0 & 1 & -1 \\ M_1 & M_2 & M_3 & M_4 \\ V_1 & V_2 & V_3 & V_4 \end{pmatrix} \begin{pmatrix} \Gamma_{pm}^w \\ \Gamma_{cm}^w \\ \Gamma_{pm}^\theta \\ \Gamma_{cm}^\theta \end{pmatrix} = \begin{pmatrix} 0 \\ 0 \\ M_5 \\ V_5 \end{pmatrix}. \tag{2.36}$$

The terms of the coefficient matrix are defined in Appendix B.

It was noted in Section 2.1 that the presence of the hyperbolic terms in the Lévy solution can lead to some numerical instability. When considering higher terms in the series, i.e., with increasing m, α_m^4 in general is greater than β^4 and the last summation term in Equations (2.19), (2.24), and (2.25) becomes the appropriate form of the solution with the corresponding system of coefficients given by Equation (B.3). With increasing m, the arguments of the hyperbolic terms become quite large and numerical evaluation of the system can lead to instability. In this situation, it becomes necessary to switch to asymptotic forms of the system to achieve a convergent and stable solution. These asymptotic limits are

$$\begin{aligned} \sinh a &\to e^a/2 \quad a > 0, \quad \sinh a \to -e^{-a}/2 \quad a < 0, \\ \cosh a &\to e^a/2 \quad a > 0, \quad \cosh a \to e^{-a}/2 \quad a < 0. \end{aligned}$$

With these limits it can be shown that $M_5 = V_5 = 0$, which leads to $\Gamma_{pm}^w = \Gamma_{cm}^w = \Gamma_{pm}^\theta = \Gamma_{cm}^\theta = 0$ and a convergent series. Note that the hyperbolic terms increase fairly rapidly, but there is a transition period where it is inappropriate to use these limits. In this transition, there is an observed loss of precision when compared to the numerically well-behaved solution of Equation (2.19).

2.6 Imperfect Conditions

Figure 2.7 demonstrates this solution without and with the introduction of a displacement gap between the $\mathcal{P}$ and $\mathcal{C}$-domains.

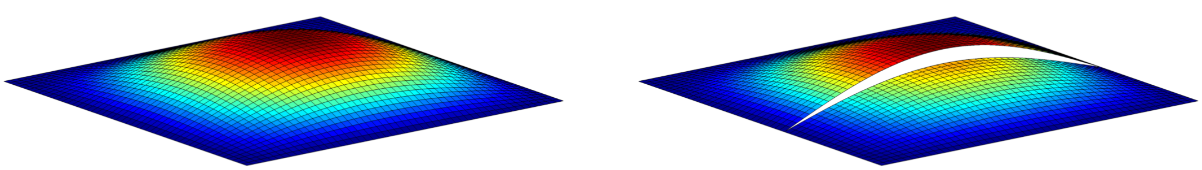

(a) Perfect matching (no error).

(b) Forced incompatibility in displacements.

Figure 2.7: Hybrid plate with a displacement gap.

Returning to the system of Equation (2.36) and re-introducing the error terms leads to

$$\begin{pmatrix} 1 & -f_w & 0 & 0 \\ 0 & 0 & 1 & -f_\theta \\ M_1 & f_w M_2 & f_M M_3 & f_\theta f_M M_4 \\ V_1 & f_w V_2 & f_V V_3 & f_\theta f_V V_4 \end{pmatrix} \begin{pmatrix} \Gamma_{pm}^w \\ \Gamma_{cm}^w \\ \Gamma_{pm}^\theta \\ \Gamma_{cm}^\theta \end{pmatrix} = \begin{pmatrix} 0 \\ 0 \\ f_M M_5 \\ f_V V_5 \end{pmatrix}. \tag{2.37}$$

with a solution given by

$$\Gamma^w_{pm} = \frac{f_M f_V[(V_3 + f_\theta V_4)M_5 - (M_3 + f_\theta M_4)V_5]}{f_V(M_1 + f_w M_2)(V_3 + f_\theta V_4) - f_M(M_3 + f_\theta M_4)(V_1 + f_w V_2)}, \tag{2.38a}$$

$$\Gamma^w_{cm} = f_w \Gamma^w_{pm}, \tag{2.38b}$$

$$\Gamma^\theta_{pm} = \frac{f_M(V_1 + f_w V_2)M_5 - f_V(M_1 + f_w M_2)V_5}{f_M(M_3 + f_\theta M_4)(V_1 + f_w V_2) - f_V(M_1 + f_w M_2)(V_3 + f_\theta V_4)}, \tag{2.38c}$$

$$\Gamma^\theta_{cm} = f_\theta \Gamma^\theta_{pm}. \tag{2.38d}$$

3. Error Analysis

To study the effect of an error introduced at the interface between the $\mathcal{P}$ and $\mathcal{C}$-domains, non-dimensional forms of the solutions are presented. An appropriate norm is then defined to describe the errors over the domain.

3.1 Non-Dimensionalization

The following non-dimensional parameters are introduced:

$$\xi = \tfrac{x}{a} \quad \eta = \tfrac{y}{b} \quad \psi = \tfrac{w}{b}, \tag{3.39a}$$

$$\eta_p = \tfrac{b_p}{b} \quad \eta_c = \tfrac{b_c}{b}, \tag{3.39b}$$

$$\Omega = \tfrac{\omega}{\bar{\omega}_{11}} \quad \tau = \bar{\omega}_{11} t \quad \bar{\mu} = \tfrac{\bar{M} b}{D}, \tag{3.39c}$$

$$\bar{\gamma}_1 = \gamma_1 b = \pi \tfrac{b}{a} \sqrt{(1 + (\tfrac{a}{b})^2)\Omega + m^2} \quad \bar{\gamma}_2 = \gamma_2 b = \pi \tfrac{b}{a} \sqrt{(1 + (\tfrac{a}{b})^2)\Omega - m^2}, \tag{3.39d}$$

$$\bar{\Gamma}^w_{pm} = \tfrac{\Gamma^w_{pm}}{b} \quad \bar{\Gamma}^w_{cm} = \tfrac{\Gamma^w_{cm}}{b}. \tag{3.39e}$$

With these expressions, Equation (2.19) can be expressed in non-dimensonal form as

$$\begin{aligned}
\psi(\xi, \eta, \tau) = & \sum_{m=1,3,\ldots}^{m_c} \psi_0 \sin(m\pi\xi) \left[\frac{\sin(\bar{\gamma}_2 \eta)}{\sin(\bar{\gamma}_2)} - \frac{\sinh(\bar{\gamma}_1 \eta)}{\sinh(\bar{\gamma}_1)} \right] e^{i\Omega\tau} \\
& + \sum_{m=m_c+1, m_c+3,\ldots}^{m_r} \psi_0' \sin(m\pi\xi) \big[\coth(\bar{\gamma}_1) \frac{\sinh(\bar{\gamma}_1 \eta)}{\sinh(\bar{\gamma}_1)} - \eta \frac{\cosh(\bar{\gamma}_1 \eta)}{\sinh(\bar{\gamma}_1)} \big] e^{i\Omega\tau} \\
& + \sum_{m=m_r+1, m_r+3,\ldots}^{\infty} \psi_0^* \sin(m\pi\xi) \left[\frac{\sinh \bar{\gamma}_2 \eta}{\sinh(\bar{\gamma}_2)} - \frac{\sinh(\bar{\gamma}_1 \eta)}{\sinh(\bar{\gamma}_1)} \right] e^{i\Omega\tau}.
\end{aligned} \tag{3.40}$$

For $\xi, \eta \in [0, 1]$ and $\tau \geq 0$ and where $m^2 < (1 + (\frac{a}{b})^2)\Omega$ for $m \leq m_c$, $m^2 = (1 + (\frac{a}{b})^2)\Omega$ for $m_c < m \leq m_r$ and $m^2 > (1 + (\frac{a}{b})^2)\Omega$ for $m > m_r$ and

$$\psi_0 = \frac{4\bar{\mu}}{m\pi(\bar{\gamma}_1^2 + \bar{\gamma}_2^2)}, \tag{3.41a}$$

$$\psi_0^* = \frac{4\bar{\mu}}{m\pi(\bar{\gamma}_1^2 - \bar{\gamma}_2'^2)}, \tag{3.41b}$$

$$\psi_0' = \frac{2\bar{\mu}}{m\pi\bar{\gamma}_1}. \tag{3.41c}$$

Similarly, Equations (2.24) and (2.25) can be expressed non-dimensionally as

$$\begin{aligned}\hat{\psi}_p(\xi,\eta,\tau) = &\sum_{m=1,3,\ldots}^{m_c} \sin(m\pi\xi)\big[\bar{B}_{pm}\sinh(\bar{\gamma}_1\eta) + \bar{D}_{pm}\sin(\bar{\gamma}_2\eta)\big]e^{i\Omega_p\tau} \\ &+ \sum_{m=m_c+1,m_c+3,\ldots}^{m_r} \sin(m\pi\xi)\big[\bar{F}_{pm}\sinh(\bar{\gamma}_1\eta) + \bar{G}_{pm}\eta\sinh(\bar{\gamma}_1\eta)\big]e^{i\Omega_p\tau} \\ &+ \sum_{m=m_r+1,m_r+3,\ldots}^{\infty} \sin(m\pi\xi)\big[\bar{J}_{pm}\sinh(\bar{\gamma}_1\eta) + \bar{L}_{pm}\sinh(\bar{\gamma}_2\eta)\big]e^{i\Omega_p\tau}.\end{aligned} \tag{3.42}$$

For $\xi \in [0,1]$, $\eta \in [0,\eta_p]$ and $\tau \geq 0$ with the non-dimensional forms of the Fourier coefficients of Equation (2.28) denoted by the overbar.

$$\begin{aligned}\hat{\psi}_c(\xi,\eta,\tau) = &\sum_{m=1,3,\ldots}^{m_c} \sin(m\pi\xi)\big[\psi_0(\cos(\bar{\gamma}_2(1-\eta)) - \cosh(\bar{\gamma}_1(1-\eta))) \\ &\qquad + \bar{B}_{cm}\sinh(\bar{\gamma}_1(1-\eta)) + \bar{D}_{cm}\sin(\bar{\gamma}_2(1-\eta))\big]e^{i\Omega_c\tau} \\ &+ \sum_{m=m_c+1,m_c+3,\ldots}^{m_r} \sin(m\pi\xi)\big[\bar{F}_{cm}\sinh(\bar{\gamma}_1(1-\eta)) \\ &\qquad + \bar{G}_{cm}(1-\eta)\cosh(\bar{\gamma}_1(1-\eta)) - \psi_0'(1-\eta)\sinh(\bar{\gamma}_1(1-\eta))\big]e^{i\Omega_c\tau} \\ &+ \sum_{m=m_r+1,m_r+3,\ldots}^{\infty} \sin(m\pi\xi)\big[\psi_0^*(\cosh(-\bar{\gamma}_2(1-\eta)) - \cosh(\bar{\gamma}_1(1-\eta))) \\ &\qquad + \bar{J}_{cm}\sinh((\bar{\gamma}_1(1-\eta)) + \bar{L}_{cm}\sinh(-\bar{\gamma}_2(1-\eta))\big]e^{i\Omega_c\tau}.\end{aligned} \tag{3.43}$$

For $\xi \in [0,1]$, $\eta \in [\eta_p,1]$ and $\tau \geq 0$ and with the non-dimensional forms of the Fourier coefficients of Equation (2.31) denoted by the overbar.

3.2 Error Norms

A L_2 displacement error norm is defined as follows for each domain:

$$||e_{pw}||^2 = \int_\tau\int_\xi\int_\eta (\psi - \hat{\psi}_p)^2 \; d\eta \; d\xi \; d\tau, \tag{3.44a}$$

$$||e_{cw}||^2 = \int_\tau\int_\xi\int_\eta (\psi - \hat{\psi}_c)^2 \; d\eta \; d\xi \; d\tau, \tag{3.44b}$$

$$||e_w|| = \sqrt{||e_{pw}||^2 + ||e_{cw}||^2}. \tag{3.44c}$$

The integrals in Equation (3.44) are to be evaluated as

$$||e_{pw}||^2 = \int_\tau\int_\xi\int_\eta \psi^2 + \hat{\psi}_p^2 - 2\psi\hat{\psi}_p \; d\eta \; d\xi \; d\tau, \tag{3.45a}$$

$$||e_{cw}||^2 = \int_\tau\int_\xi\int_\eta \psi^2 + \hat{\psi}_c^2 - 2\psi\hat{\psi}_c \; d\eta \; d\xi \; d\tau. \tag{3.45b}$$

With reference to Appendix C, the final form of these integrals can be expressed as

$$||e_{pw}||^2 = \frac{\pi}{2\Omega} \sum_{m=1,3,\ldots}^{M} \left(\int_0^{\eta_p} Y_m^2 \, d\eta + \int_0^{\eta_p} \mathrm{Re}(Y_{pm})^2 + \mathrm{Im}(Y_{pm})^2 \, d\eta - 2 \int_0^{\eta_p} Y_m \, \mathrm{Re}(Y_{pm}) \, d\eta \right), \tag{3.46a}$$

$$||e_{cw}||^2 = \frac{\pi}{2\Omega} \sum_{m=1,3,\ldots}^{M} \left(\int_{\eta_p}^{1} Y_m^2 \, d\eta + \int_{\eta_p}^{1} \mathrm{Re}(Y_{cm})^2 + \mathrm{Im}(Y_{cm})^2 \, d\eta - 2 \int_{\eta_p}^{1} Y_m \, \mathrm{Re}(Y_{cm}) \, d\eta \right), \tag{3.46b}$$

where the spatial integration has been carried out over the domain of the plate and the time integration over one period of the harmonic excitation. Y_m, Y_{pm}, and Y_{cm} are given in Equations (3.40), (3.42), and (3.43), respectively. It is useful to consider other norms related to different quantities of interest, primarily the rotation, bending moment, and shear. The strategy of Appendix C can be adopted to compute these norms given the proper integrands. For instance, the rotation L_2 error norm can be computed as

$$||e_{p\theta}||^2 = \frac{\pi}{2\Omega} \sum_{m=1,3,\ldots}^{M} \left(\int_0^{\eta_p} Y'^2_m \, d\eta + \int_0^{\eta_p} \mathrm{Re}(Y'_{pm})^2 + \mathrm{Im}(Y'_{pm})^2 \, d\eta - 2 \int_0^{\eta_p} Y'_m \, \mathrm{Re}(Y'_{pm}) \, d\eta \right), \tag{3.47a}$$

$$||e_{c\theta}||^2 = \frac{\pi}{2\Omega} \sum_{m=1,3,\ldots}^{M} \left(\int_{\eta_p}^{1} Y'^2_m \, d\eta + \int_{\eta_p}^{1} \mathrm{Re}(Y'_{cm})^2 + \mathrm{Im}(Y'_{cm})^2 \, d\eta - 2 \int_{\eta_p}^{1} Y'_m \, \mathrm{Re}(Y'_{cm}) \, d\eta \right), \tag{3.47b}$$

$$||e_\theta|| = \sqrt{||e_{p\theta}||^2 + ||e_{c\theta}||^2}, \tag{3.47c}$$

where $Y' = dY/d\eta$. Similar expressions can be used to determine the bending moment L_2 error norm, $||e_M||$, and the shear L_2 error norm, $||e_V||$. It is perhaps more useful to consider the relative errors with respect to the true solution. The error norms considered for the following error analysis are of the form given by Equation (3.48):

$$||e_w||_{rel} = ||e_w||/||\psi||, \tag{3.48a}$$
$$||e_\theta||_{rel} = ||e_\theta||/||\theta_y||, \tag{3.48b}$$
$$||e_M||_{rel} = ||e_M||/||M_y||, \tag{3.48c}$$
$$||e_V||_{rel} = ||e_V||/||V_y||, \tag{3.48d}$$

where the non-hybrid norms can be expressed similar to Equation (3.46). The definitions of the bending moment and shear in Appendix A [Timoshenko 1959] are used to arrive at the following expressions:

$$||\psi|| \;= \frac{\pi}{2\Omega} \sum_{m=1,3,...}^{M} \left(\int_0^1 Y_m^2 \; d\eta \right), \tag{3.49a}$$

$$||\theta_y|| \;= \frac{\pi}{2\Omega} \sum_{m=1,3,...}^{M} \left(\int_0^1 {Y'}_m^2 \; d\eta \right), \tag{3.49b}$$

$$||M_y|| = \frac{\pi}{2\Omega} \sum_{m=1,3,...}^{M} \left(\int_0^1 ({Y''}_m - \nu (m\pi)^2 Y_m)^2 \; d\eta \right), \tag{3.49c}$$

$$||V_y|| \;= \frac{\pi}{2\Omega} \sum_{m=1,3,...}^{M} \left(\int_0^1 ({Y'''}_m - (1-2\nu)(m\pi)^2 {Y'}_m)^2 \; d\eta \right), \tag{3.49d}$$

where $Y'' = d^2Y/d\eta^2$ and $Y''' = d^3Y/d\eta^3$.

3.3 Parametric Study of Errors

For the purpose of illustration in this section, material properties of steel are chosen with Poisson's ratio $\nu = 0.3$. Square plates ($a/b = 1$) with thickness ratio $h/b = 0.1$ are presented.

3.3.1 Perfect Conditions: No Error

Figure 3.1 shows a frequency sweep of the norms introduced in the preceding section over a range of driving frequencies of interest. Zero error is introduced between the $\mathcal{P}$ and $\mathcal{C}$-domains. Other parameters are held constant. Several important observations are noted as follows:

1. The relative "zero" error is above the machine precision. As discussed in Section 2.5, the use of the hyperbolic terms in the series leads to a noticeable loss of precision. There is significant oscillation in the resulting norms as the frequency is changed. This is due to the attempted numerical evaluation of "zero" with finite machine precision.

2. The higher order norms (i.e., rotation, bending moment and shear) are subject to a higher loss of precision (due to the relative complexity of numerical evaluation) when compared to the displacement norm. Furthermore, a downward trend can be seen with increasing frequency, which is not observed with the displacement norm.

3. Certain natural frequencies of the plate may not be excited. This stems from the excitation being in the form of a directional edge bending moment that does not activate certain symmetric modes. Mathematically speaking, the "missing" natural frequencies only appear in even terms of the series solution, with the solution here being an odd series. This is observed at $\Omega = 4$.

The integrals in Equation (3.46) may be evaluated analytically or numerically with the use of high-order numerical quadrature. The analytical expressions involve large operations with increasing hyperbolic terms that lead to significant loss of precision and render them surprisingly less accurate than numerical quadrature. The use of Gauss-Kronrod numerical quadrature with well-defined error bounds [Kronrod 1965] provides more favorable results and is used in this study unless otherwise noted.

Figure 3.2 demonstrates the effect of the separation location (i.e., η_p) on the error norms with no introduced errors, comparing both analytical and numerical integration. In Figure 3.2a, the relative tolerance used to determine the switch to the asymptotic forms is set relatively high (10^{-5}), and the integration methods provide essentially identical results. Figure 3.2b tightens the tolerance and the analytical integration begins to accumulate error due to loss of precision. Indeed, as the tolerance is lowered to machine precision, the numerical integrations converges while the analytical integration exhibits large errors (Figure 3.2c). There is an upward trend of the norm with increasing η_p that is accompanied by sudden drops at discrete values of η_p, leading to an overall downward trend of the norm. These are artifacts of the finite numerical precision when attempting to evaluate "zero." These trends are not present when there is a gap and can be observed in Figure 3.14 as part of a later discussion.

It is concluded that the behavior of the full plate can be captured fairly accurately by the formulation presented for the hybrid plate. The error analysis presented in this chapter will be made with reference to the "zero" error solution being the perfect case.

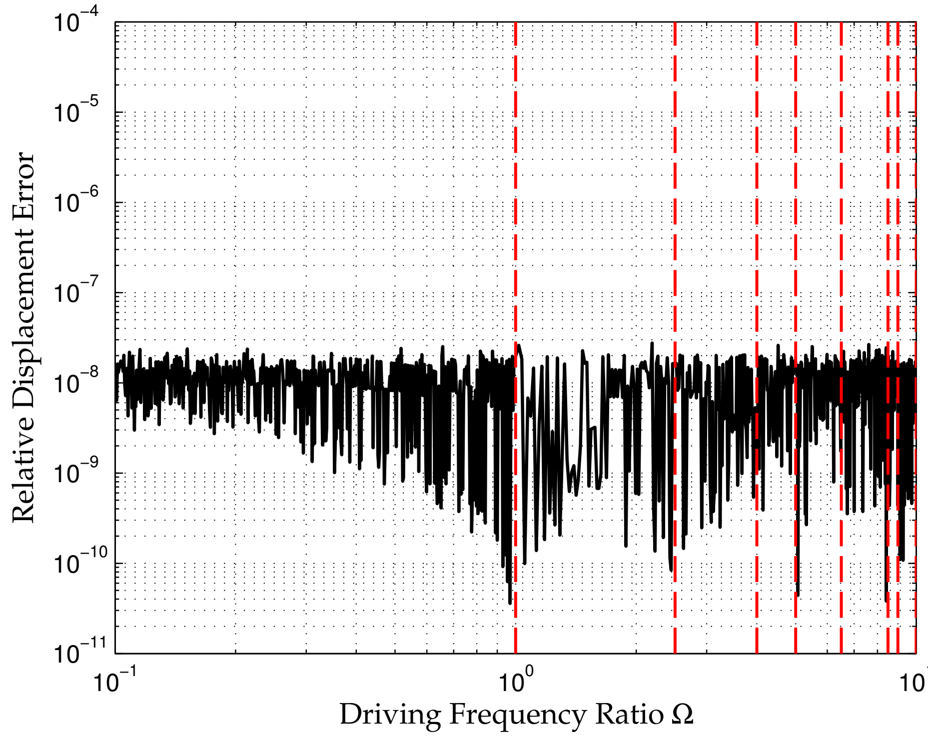

(a) Relative displacement error

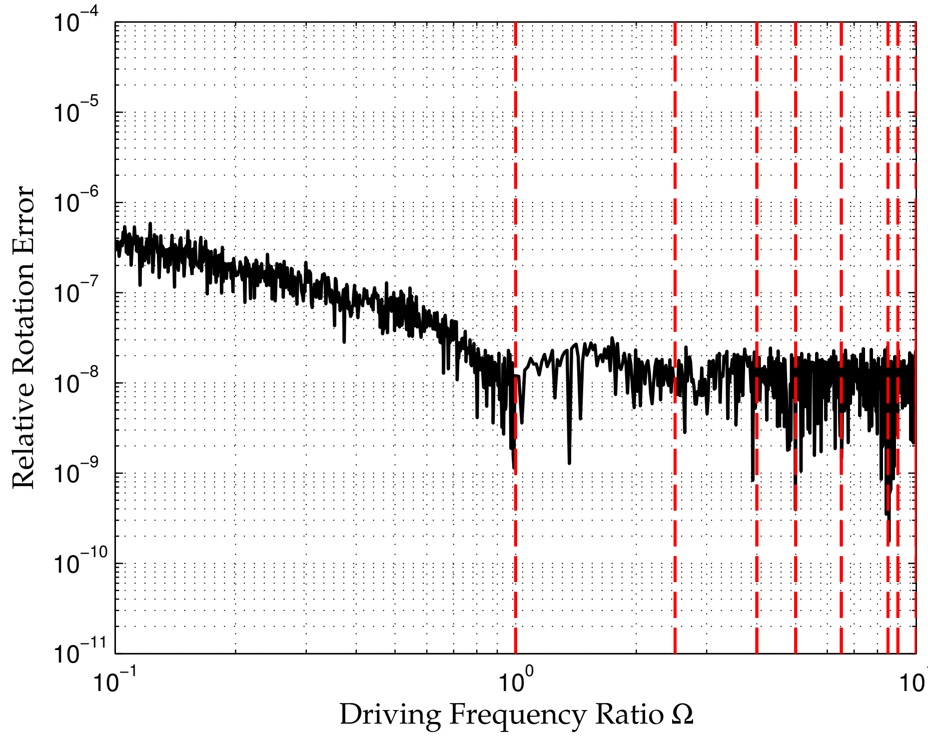

(b) Relative rotation error

Figure 3.1: Frequency sweep of relative errors under perfect domain matching. Natural frequencies are shown as dashed lines but omitted from the plots for clarity.

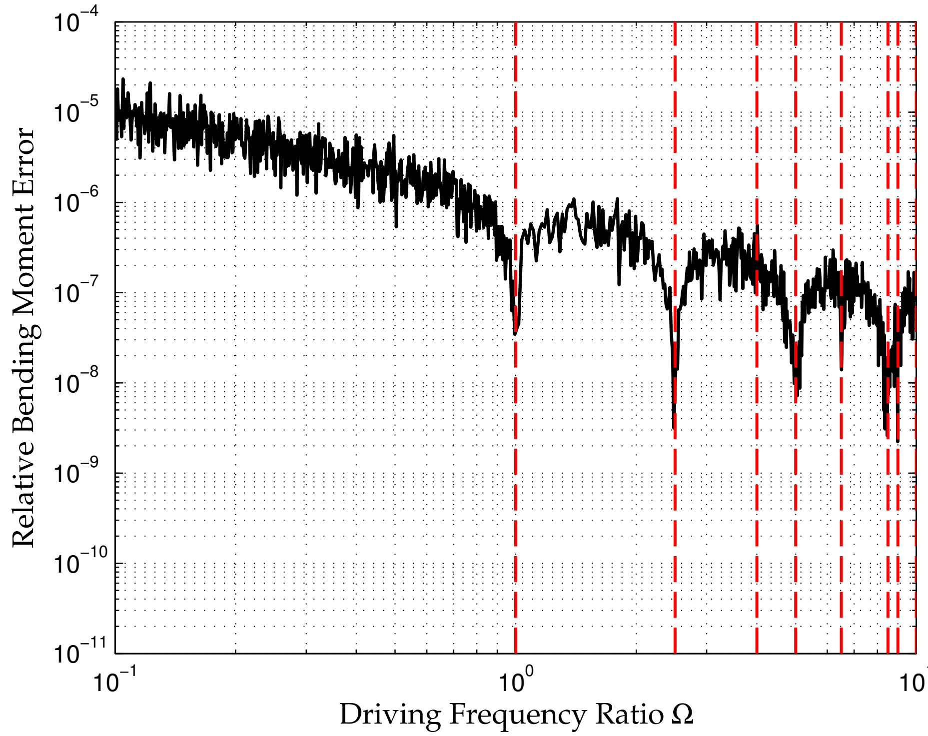

(c) Relative bending moment error

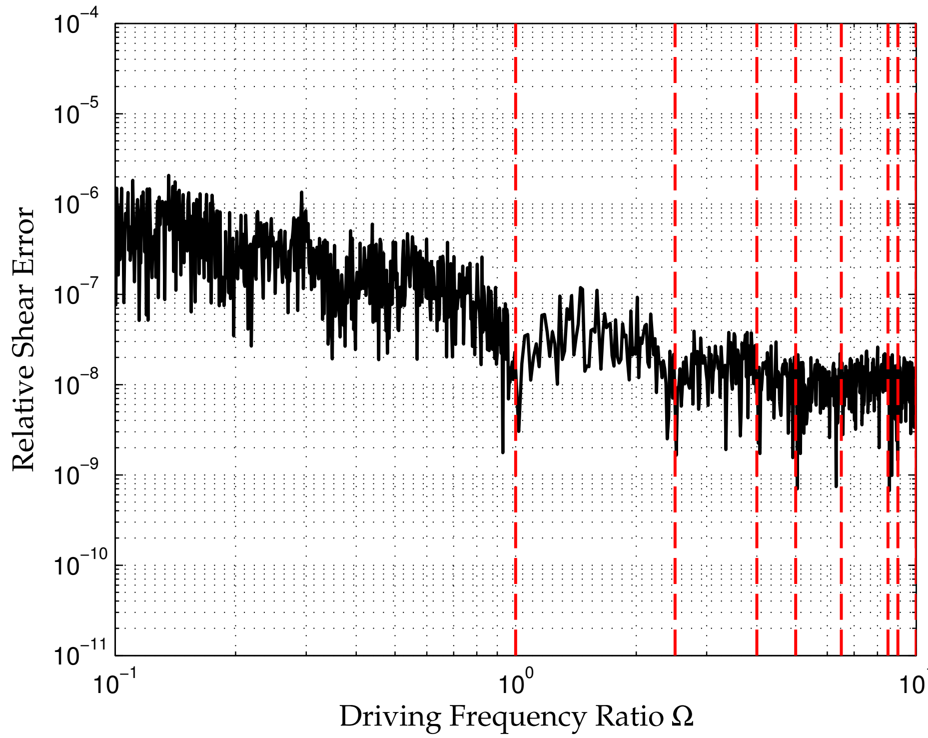

(d) Relative shear error

Figure 3.1 (Cont.): Frequency sweep of relative errors under perfect domain matching. Natural frequencies are shown as dashed lines but omitted from the plots for clarity.

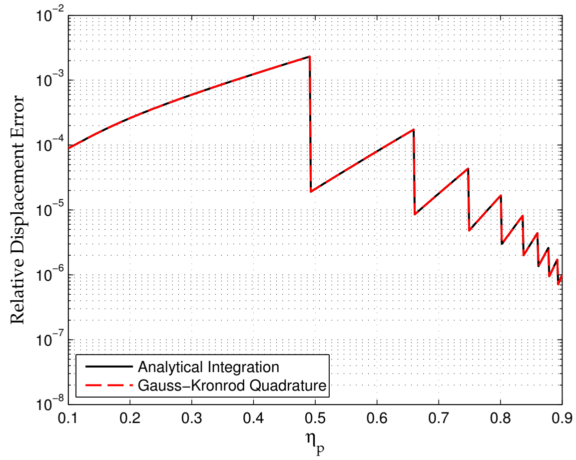

(a) Relative tolerance of switch to asymptotic forms: 10^{-5}

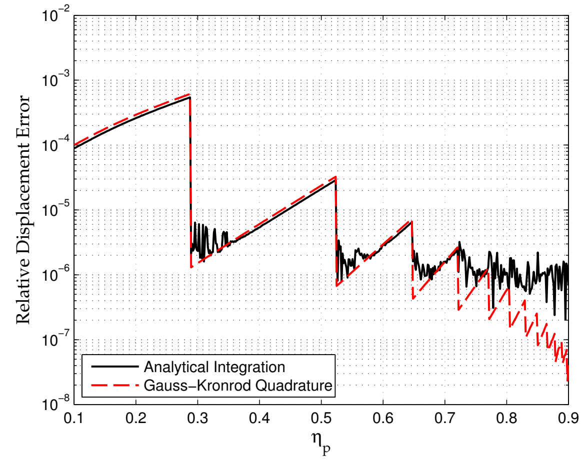

(b) Relative tolerance of switch to asymptotic forms: 10^{-7}

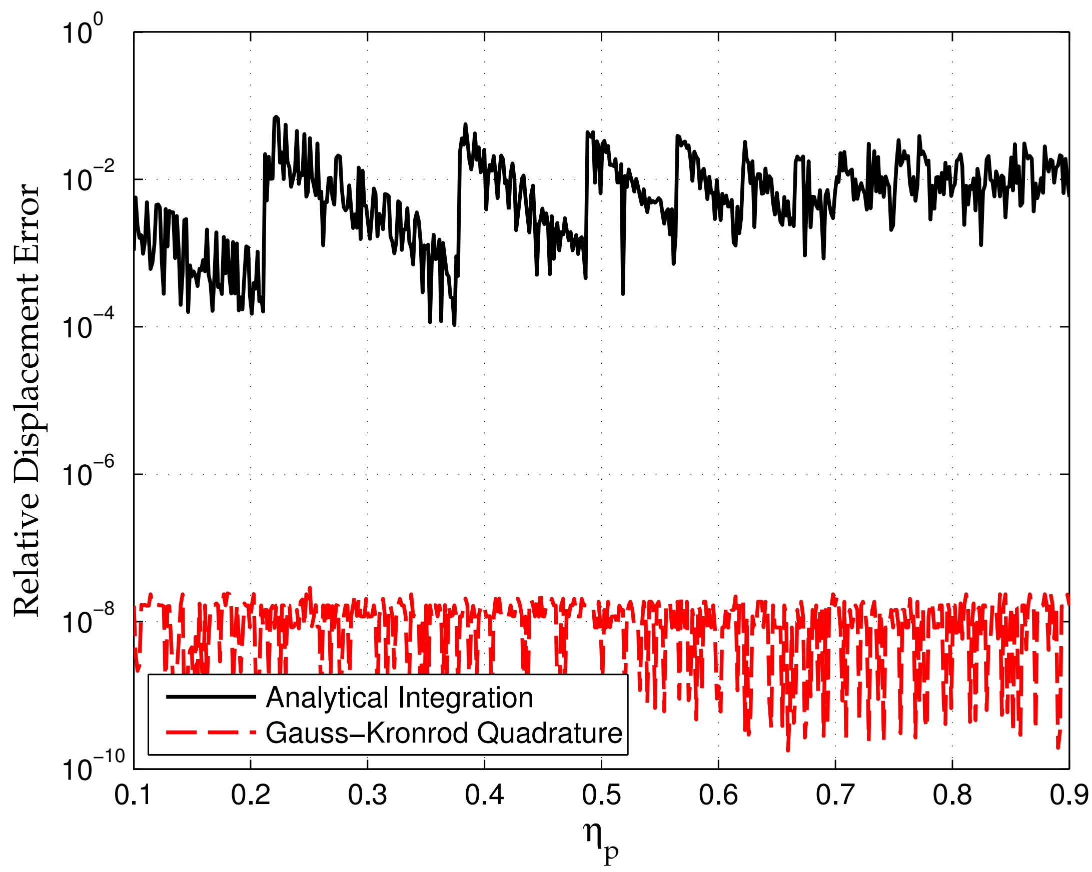

(c) Relative tolerance of switch to asymptotic forms: 10^{-16}

Figure 3.2: Effect of separation location on norm for perfect conditions with a comparison of exact and numerical integration.

3.3.2 Imperfect Conditions: Displacement Gap

There are four types of gaps that can be introduced into the plate, as demonstrated by Equation (2.37). The gap error terms are given by Equation (2.7). Figure 3.3 demonstrates the effect of an in-phase gap, or $\delta_k = 0$. When compared to Figure 3.1, it is apparent that across all frequencies there is a considerable increase in the relative norm. Figure 3.4 presents the same frequency sweep at a 5% magnitude error ($\varepsilon = 0.05$) but with a nonzero δ_k. The following is observed:

1. The oscillations in Figure 3.1 are not present. Instead there is a smooth response when not in the vicinity of a natural frequency.
2. The norm increases rapidly with the initial introduction of error but becomes quickly indifferent to increasing error. This is discussed further in the last part of this section.
3. Except for minor variations, under the presence of constant magnitude error and no phase delay, the four norms are very close to each other. This is different from that shown in Figure 3.1 where there was a higher loss of precision observed for the higher order norms.
4. There is a tendency to accumulate more error in the vicinity of excited natural frequencies.
5. There are frequencies that are not natural frequencies of the system that exhibit larger errors (for this case, $\Omega \approx 1.79$ and 5.58). A study of these frequencies indicates they are in fact natural frequencies of one of the sub-plates. This is discussed further in Section 3.6.
6. The error does not noticeably change below the fundamental frequency but rapidly changes near and above it.

Figure 3.4 demonstrates the same displacement gaps as in Figure 3.3 but with $\delta_k = 0.01$. The observations noted above are seen again under the presence of a time delay. The delay seems to have a larger effect on the overall response at the higher frequencies.

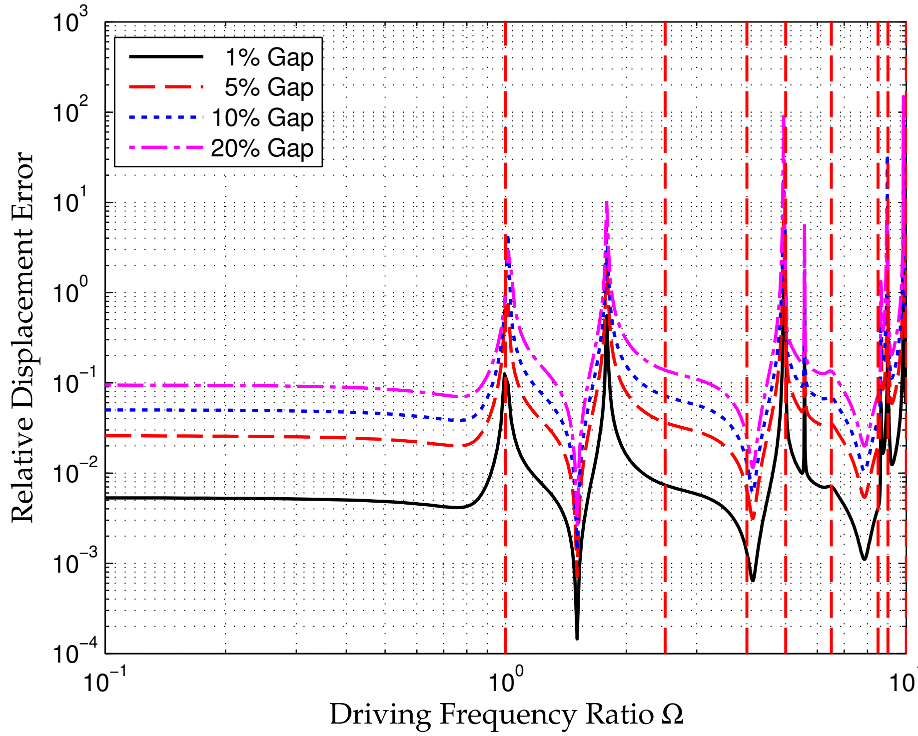

(a) Relative displacement error

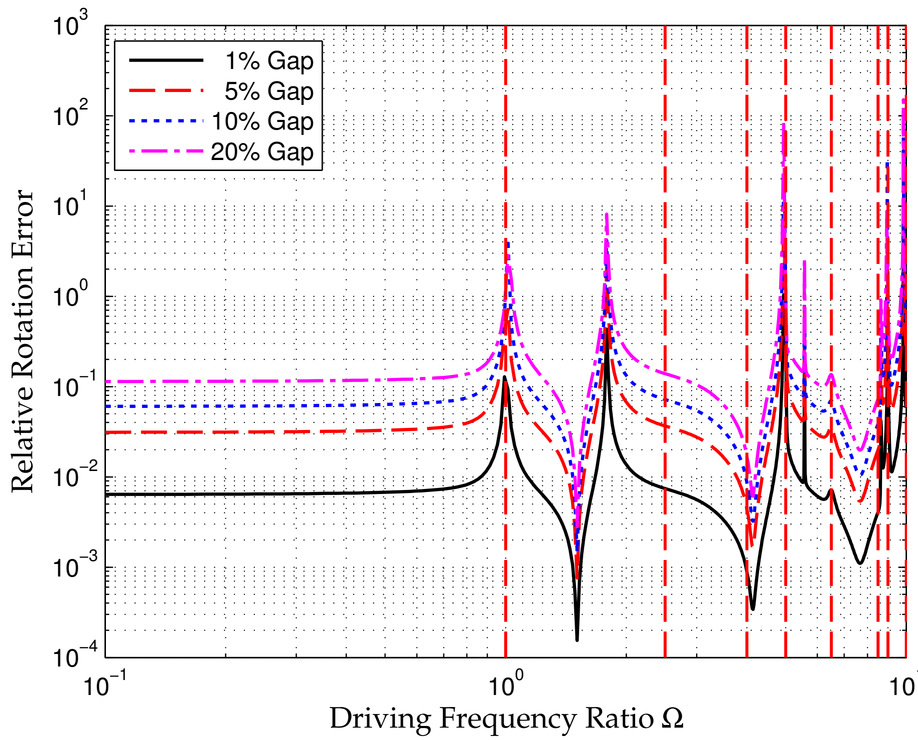

(b) Relative rotation error

Figure 3.3: Introduction of a constant magnitude displacement gap between $\mathcal{P}$ and $\mathcal{C}$-domains.

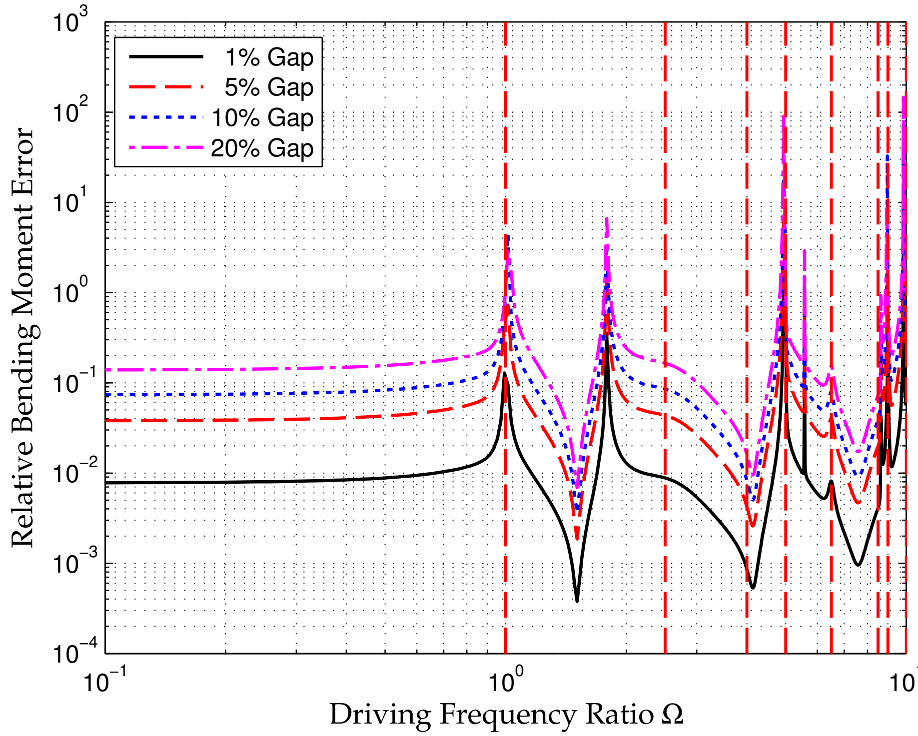

(c) Relative bending moment error

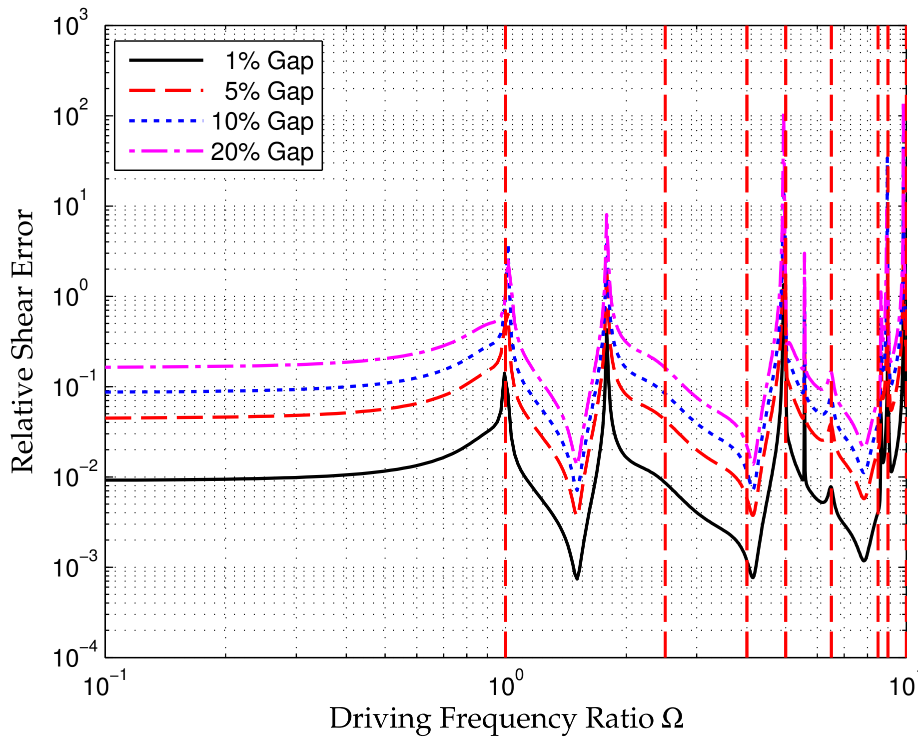

(d) Relative shear error

Figure 3.3 (Cont.): Introduction of a constant magnitude displacement gap between $\mathcal{P}$ and $\mathcal{C}$-domains.

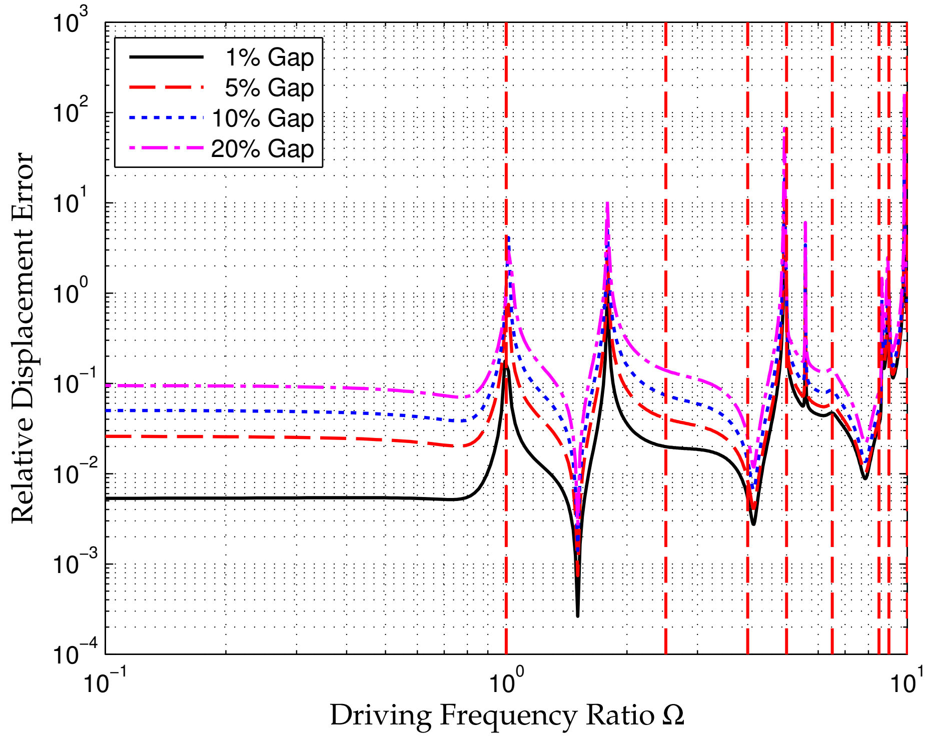

(a) Relative displacement error

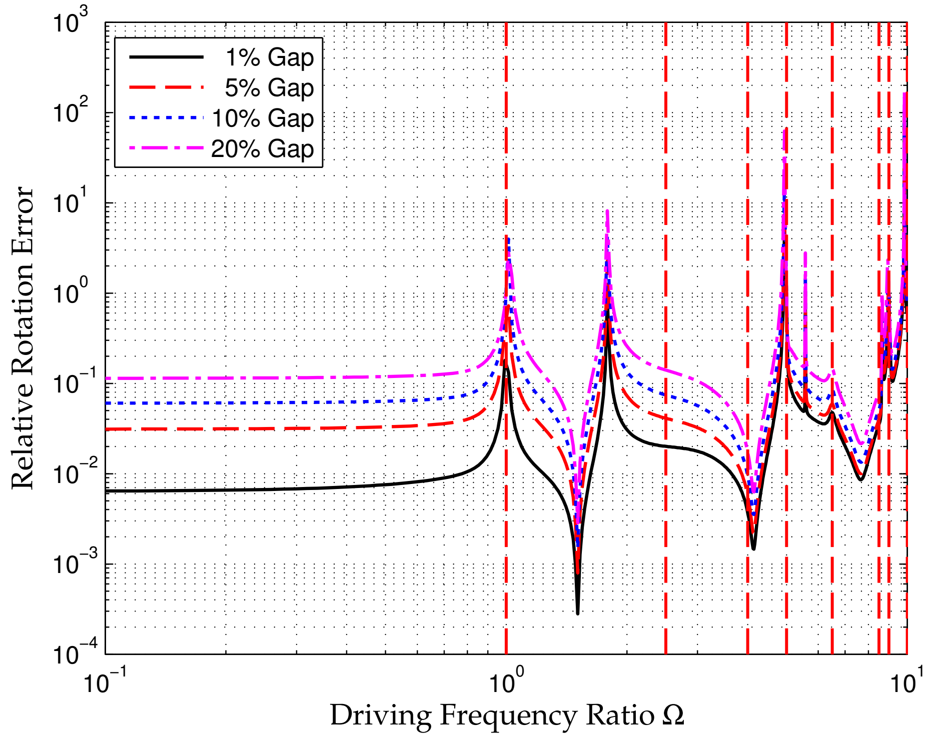

(b) Relative rotation error

Figure 3.4: Introduction of a displacement gap between $\mathcal{P}$ and $\mathcal{C}$-domains, with $\delta_k = 0.01$.

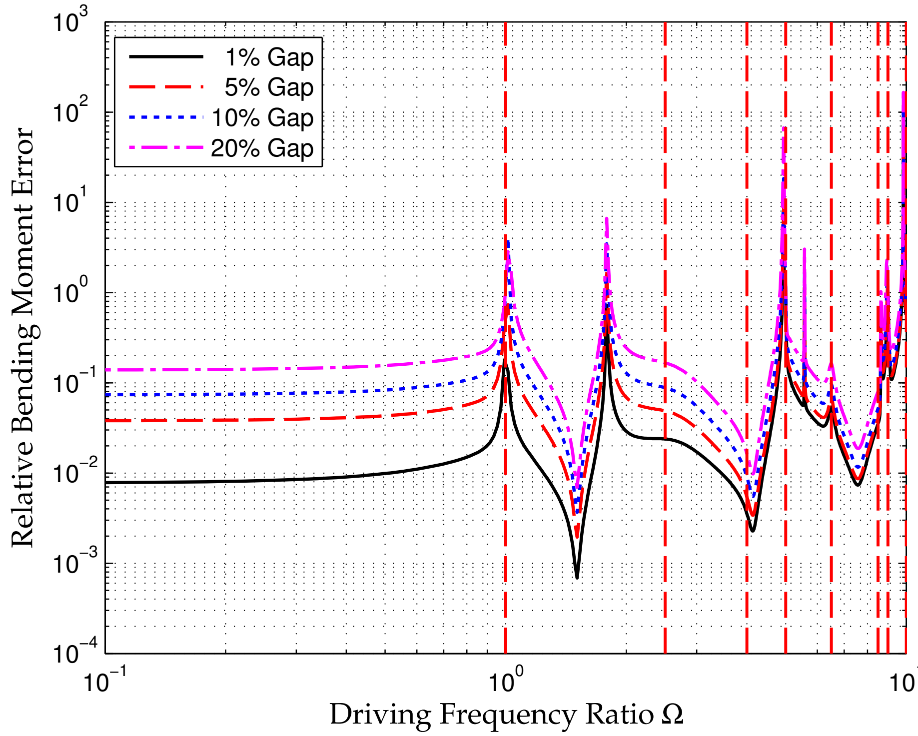

(c) Relative bending moment error

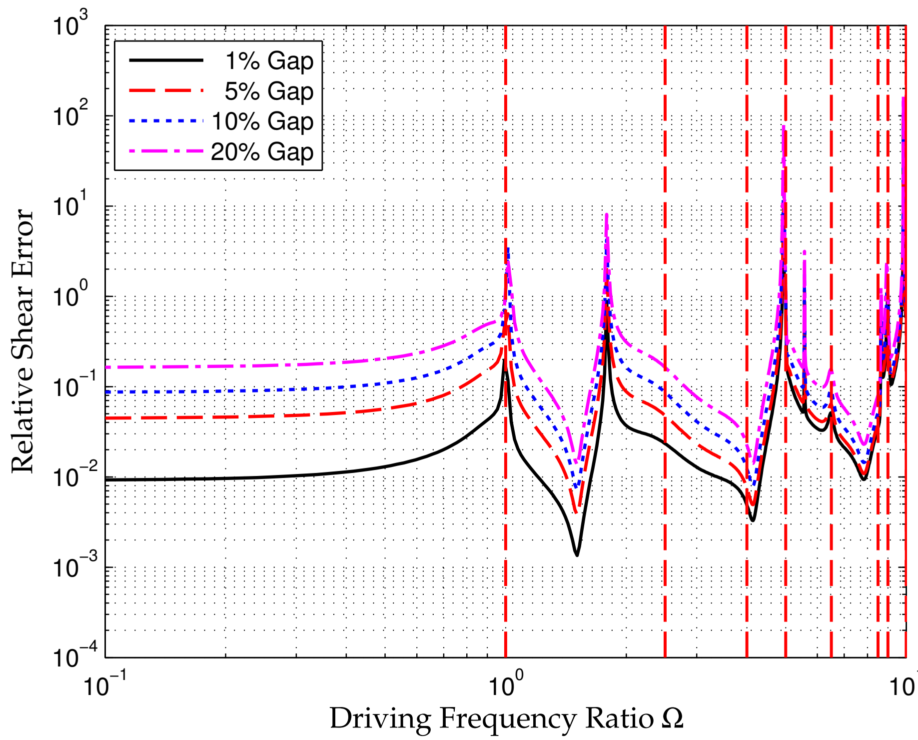

(d) Relative shear error

Figure 3.4 (Cont.): Introduction of a displacement gap between $\mathcal{P}$ and $\mathcal{C}$-domains, with $\delta_k = 0.01$.

3.3.3 Imperfect Conditions: Displacement, Rotation, Bending Moment and Shear Gaps

The gap introduced in the previous section was only in the displacement; however, the form of Equation (2.36) allows the introduction of rotation, bending moment, and shear gaps simultaneously with a displacement gap. Physically speaking, the controller not only sends and receives displacement commands but also records force response. Furthermore, the system may require imposing rotations and measuring the corresponding bending moment or torque. Therefore, naturally a hybrid system will exhibit gaps in all quantities considered across the interface. It is, however, unclear what the relative magnitude of these gaps should be. For the purpose of this study, the error introduced in each of the terms is identical and incremented simultaneously. Furthermore, due to the similarity of the different norms, only results for the displacement norm are presented.

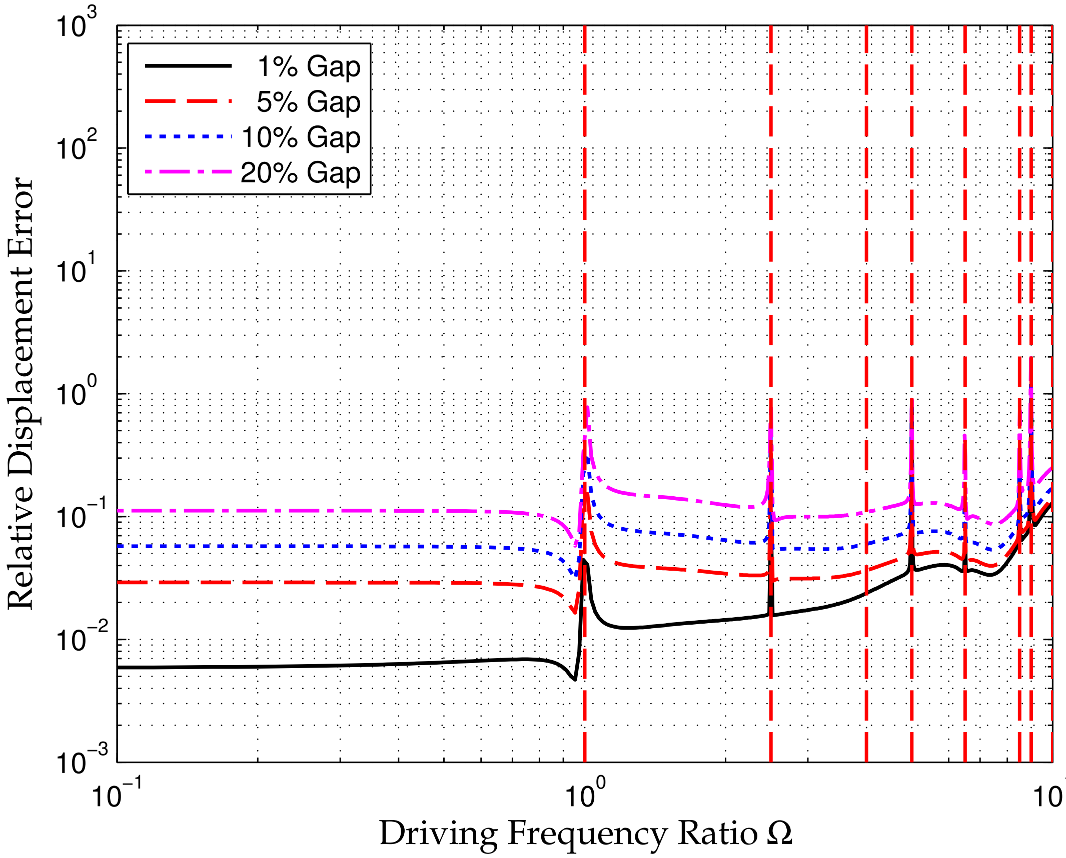

(a) Displacement and rotation gap.

Figure 3.5: Effect of multiple gaps.

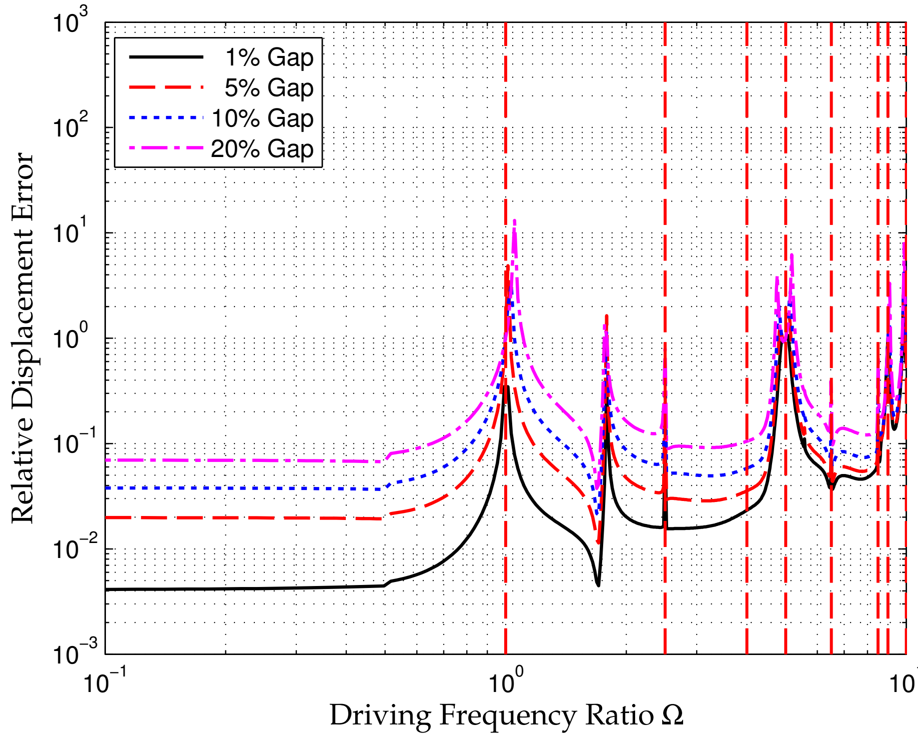

(b) Displacement, rotation, and bending moment gap

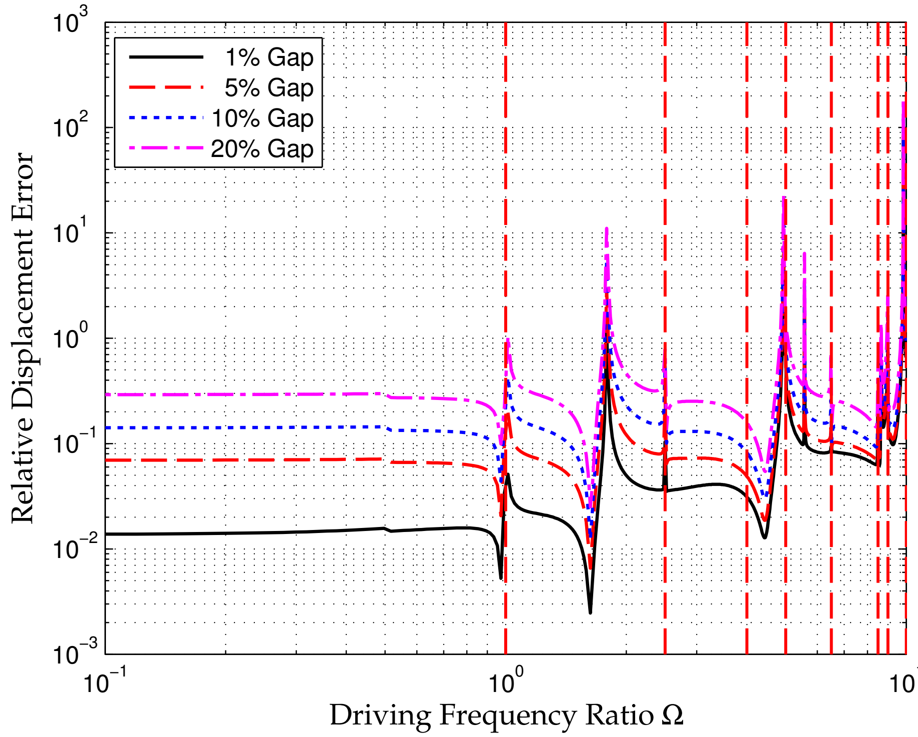

(c) Displacement, rotation, bending moment, and shear gap.

Figure 3.5 (Cont.): Effect of multiple gaps.

The effect on the overall error of multiple gaps will be considered in the next subsection. Interestingly, the frequencies described in item 5 of the previous subsection that exhibit large errors are not present with the addition of a rotation gap to the displacement gap; however, these errors return with the addition of bending moment and shear gaps. These frequencies are considered further in Section 3.6.

3.3.4 Imperfect Conditions: Effect of Increasing Gaps

The effect of increasing gap errors is now considered. The driving frequency is chosen from Figure 3.3 such that there is no excessive error and subsequently held constant. Two cases are presented: Figures 3.6a, 3.7a, and 3.8a are driven at a relatively low frequency (half of the fundamental frequency), and Figures 3.6b, 3.7b, and 3.8b are driven at a higher frequency (twice the fundamental frequency). Figure 3.7 includes a time delay, while Figure 3.8 shows the the effect of an increasing time delay. Each curve represents the error in each of the global response quantities (i.e., $||e_w||_{rel}$, $||e_\theta||_{rel}$, $||e_M||_{rel}$ and $||e_Q||_{rel}$). The following is observed:

1. As noted earlier, there is a rapid increase in the error at the first introduction of a gap, but as the gap increases, the overall response does not change significantly.

2. At low frequencies, more error is seen in the displacement and rotation response than in the shear and bending moment, as opposed to higher frequencies when the different quantities become less spread out.

3. Even with a zero magnitude gap, a time delay (phase error) induces significant errors (Figure 3.7). Physically speaking, the errors accumulate with time.

4. The phase error term, δ_k, has a more significant impact on the response than the magnitude term, ε_k, as observed in Figure 3.8.

5. There is more error observed in the kinematic quantities (displacements and rotations) than in the force quantities (bending moments and shears).

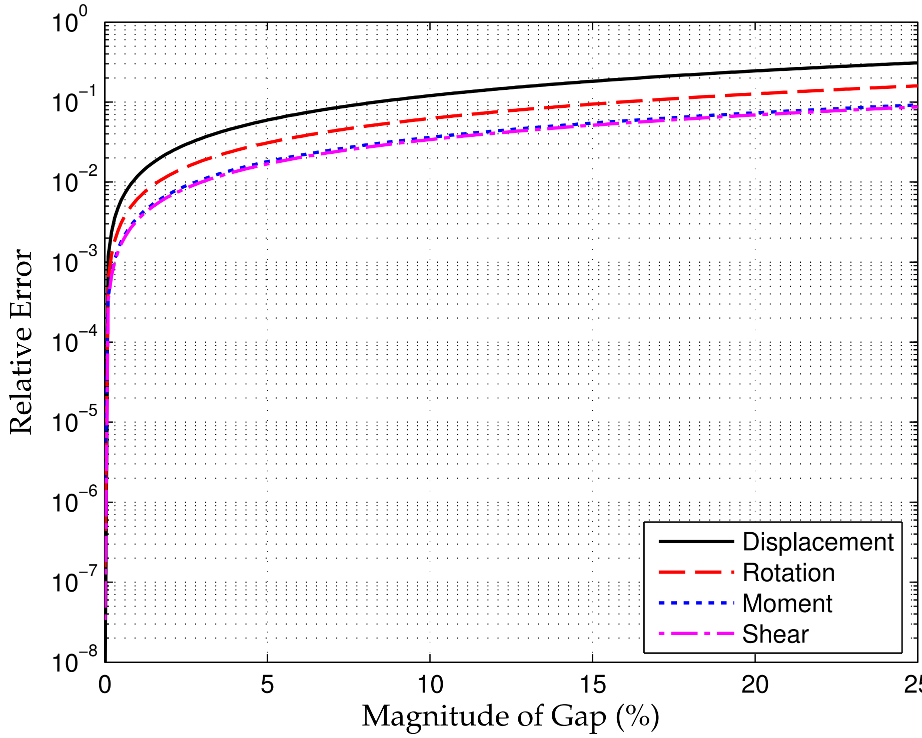

(a) $\Omega = 0.5$

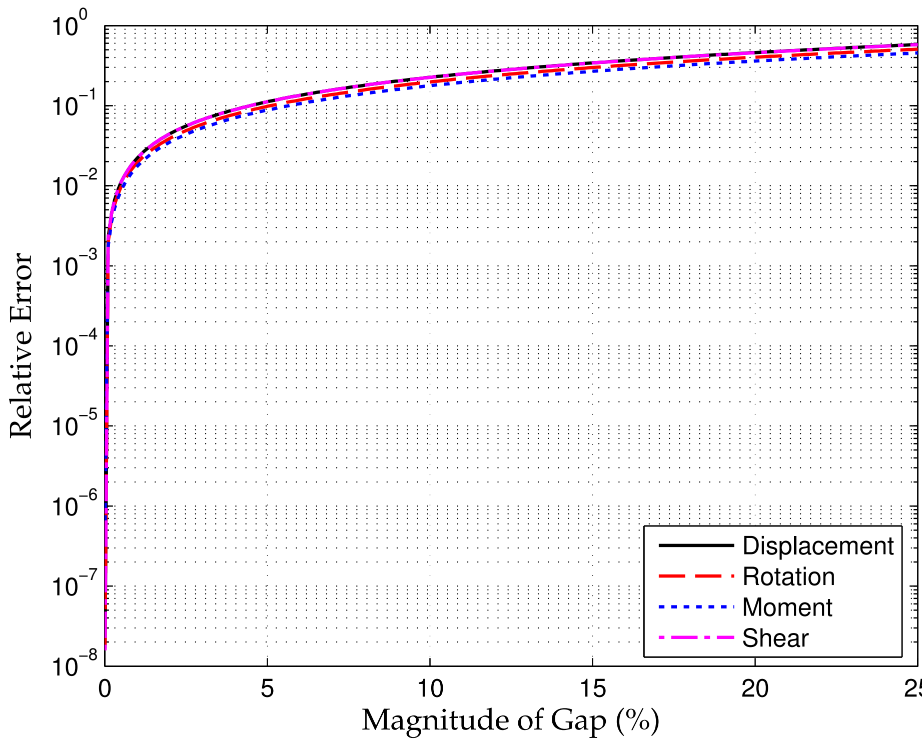

(b) $\Omega = 2$

Figure 3.6: Effect on plate response quantities with constant magnitude error gaps in displacement, rotation, bending moment, and shear with $\delta_k = 0$. All gaps are equivalent in magnitude and incremented simultaneously.

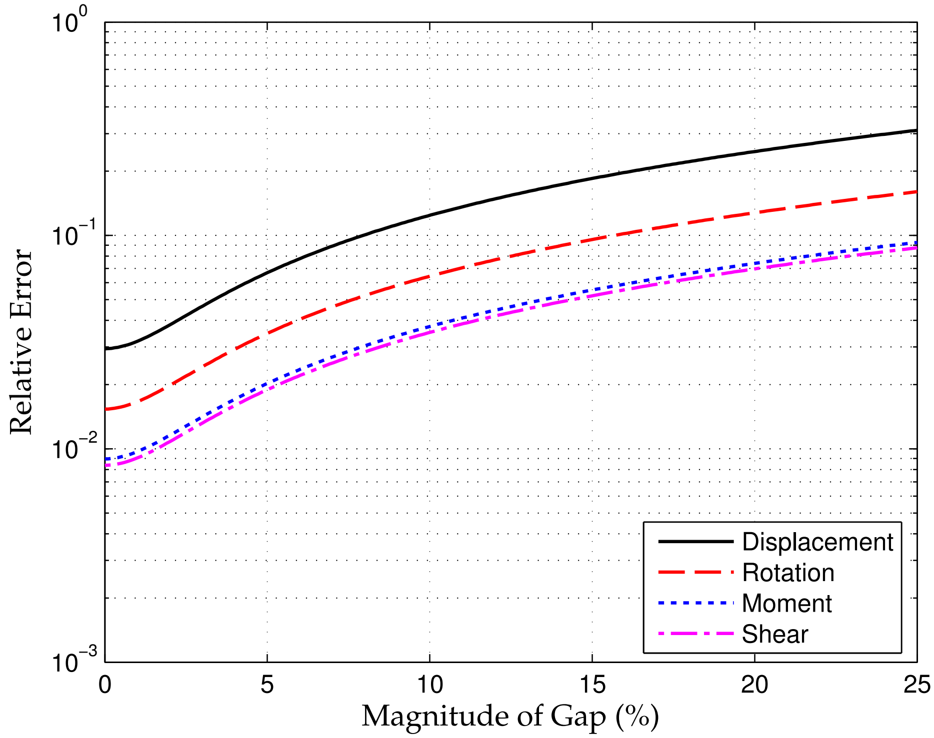

(a) $\Omega = 0.5$

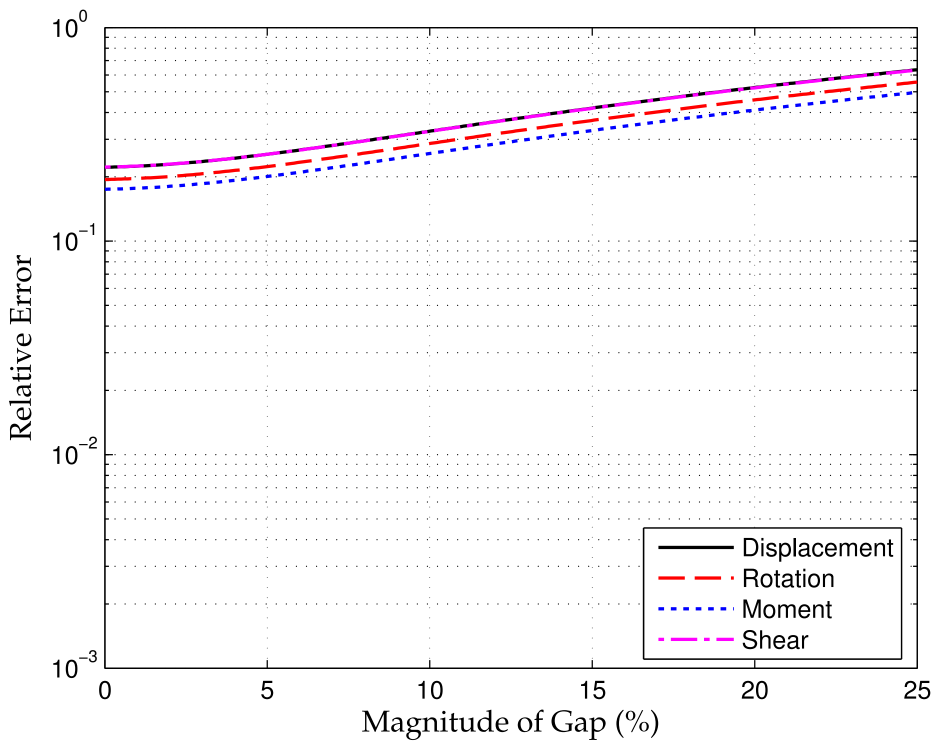

(b) $\Omega = 2$

Figure 3.7: Effect of constant magnitude error gaps in displacement, rotation, bending moment, and shear with $\delta_k = 0.05$. All gaps are equivalent in magnitude and incremented simultaneously.

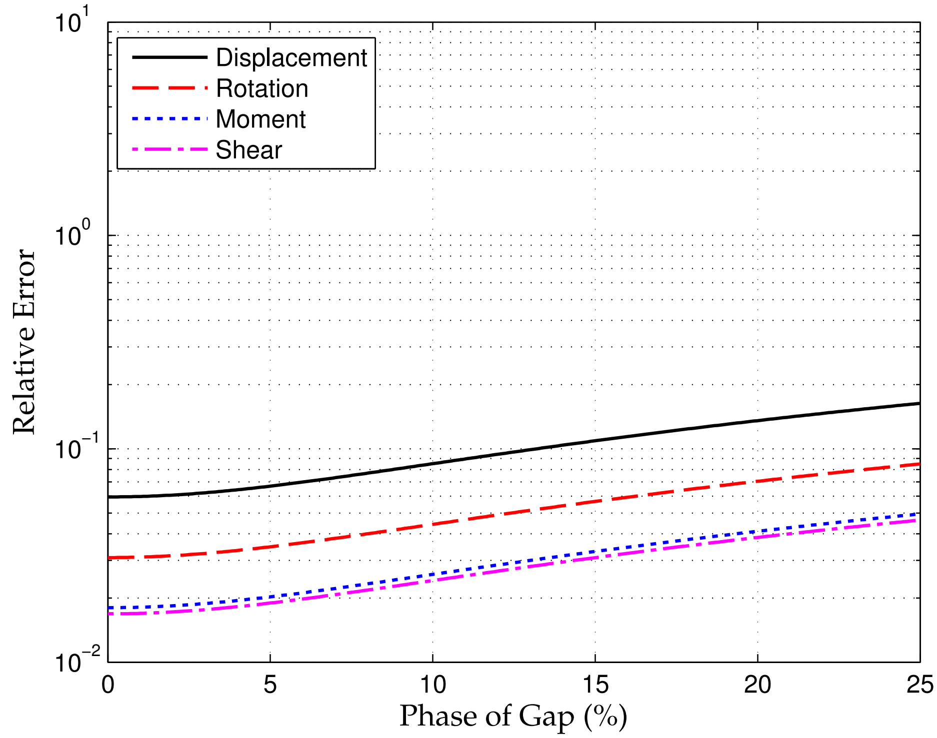

(a) $\Omega = 0.5$

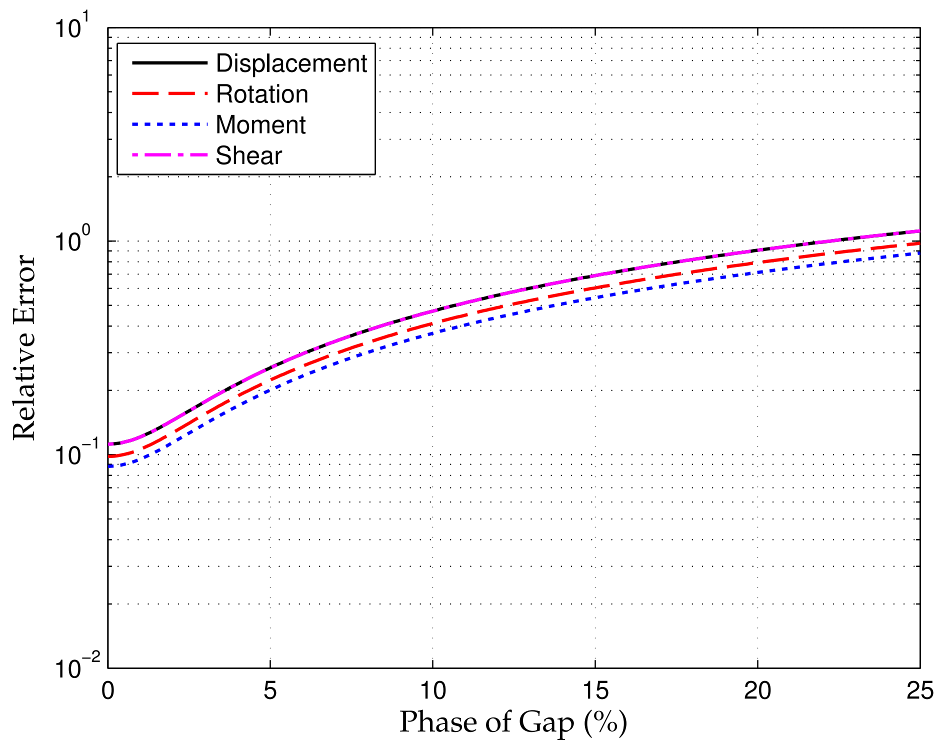

(b) $\Omega = 2$

Figure 3.8: Effect of increasing time delay.

3.4 Frequency-Dependant Errors

Making use of Equation (2.8), the effect of a frequency dependent errors is considered. Figure 3.9 demonstrates a comparison of an increasing maximum gap ε_0 as given by Equation (2.8) with $\delta_k = 0.01$. A clear upward trend shows that as the driving frequency grows, so does the error. Furthermore, there is little difference in the error of the various response quantities. Finally, the effect of ε_0 is only significant at higher frequencies.

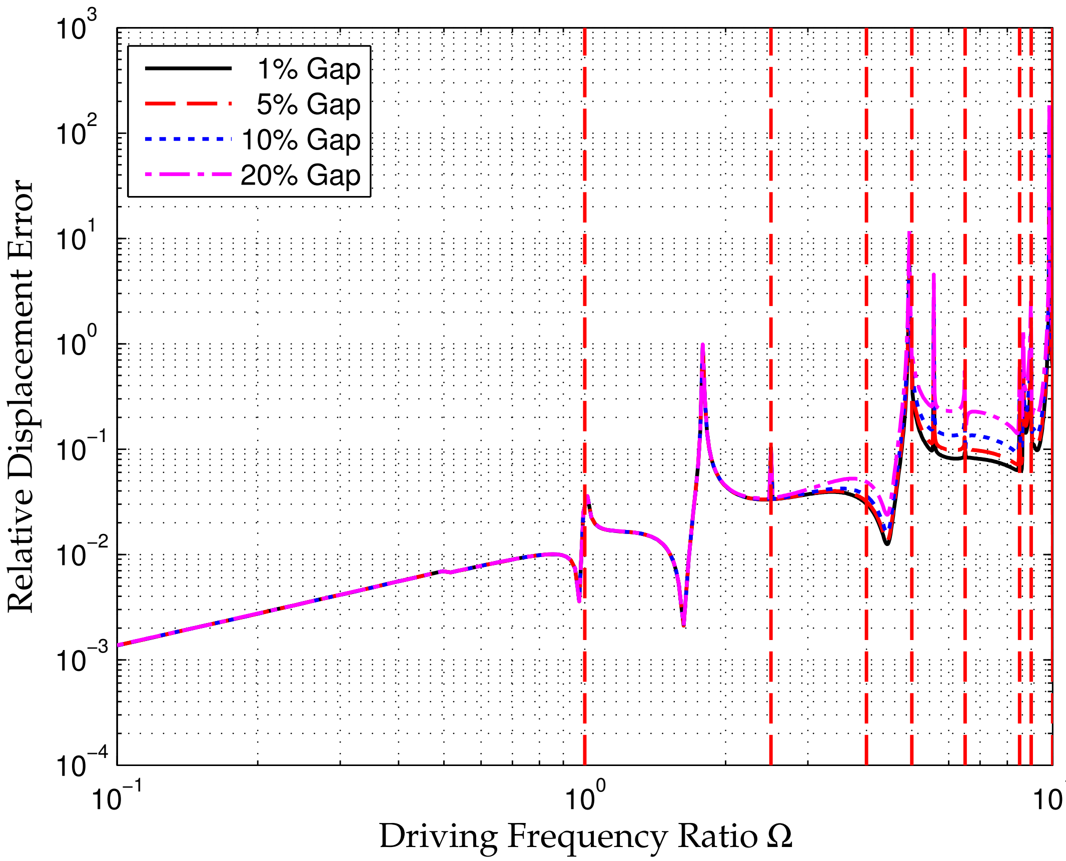

(a) Relative displacement error

Figure 3.9: Frequency dependent gaps with $\delta_k = 0.01$ in displacement, rotation, bending moment, and shear.

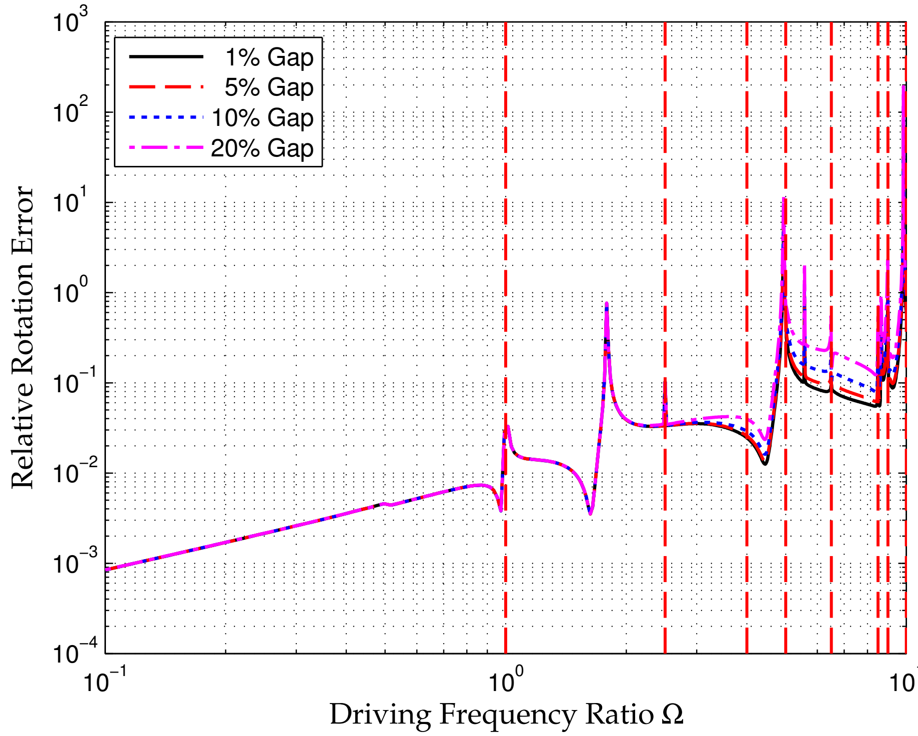

(b) Relative rotation error

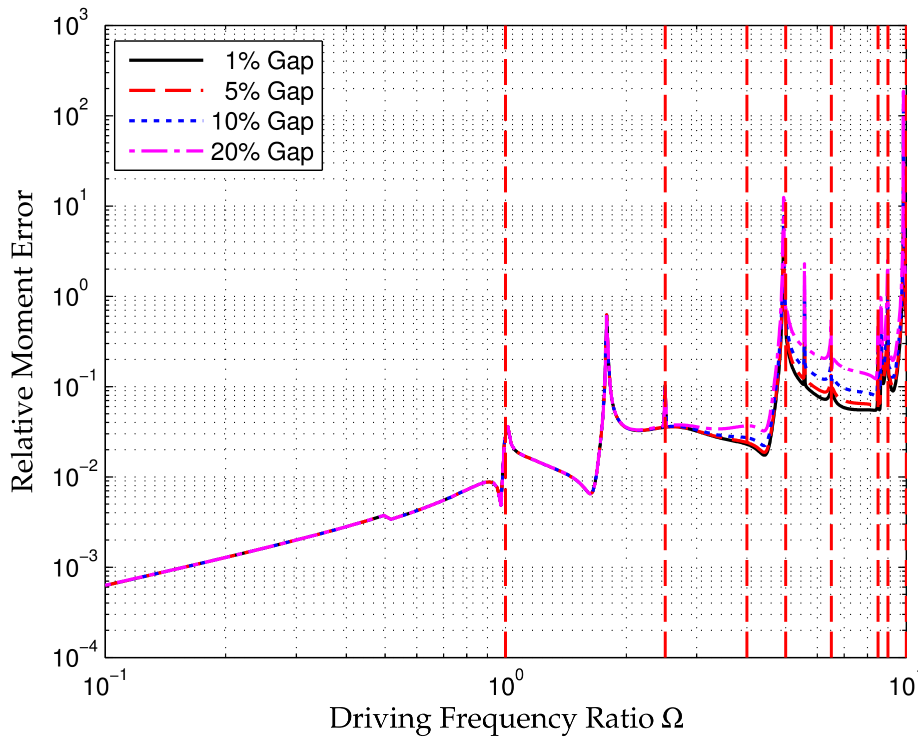

(c) Relative bending moment error

Figure 3.9 (Cont.): Frequency dependent gaps with $\delta_k = 0.01$ in displacement, rotation, bending moment, and shear.

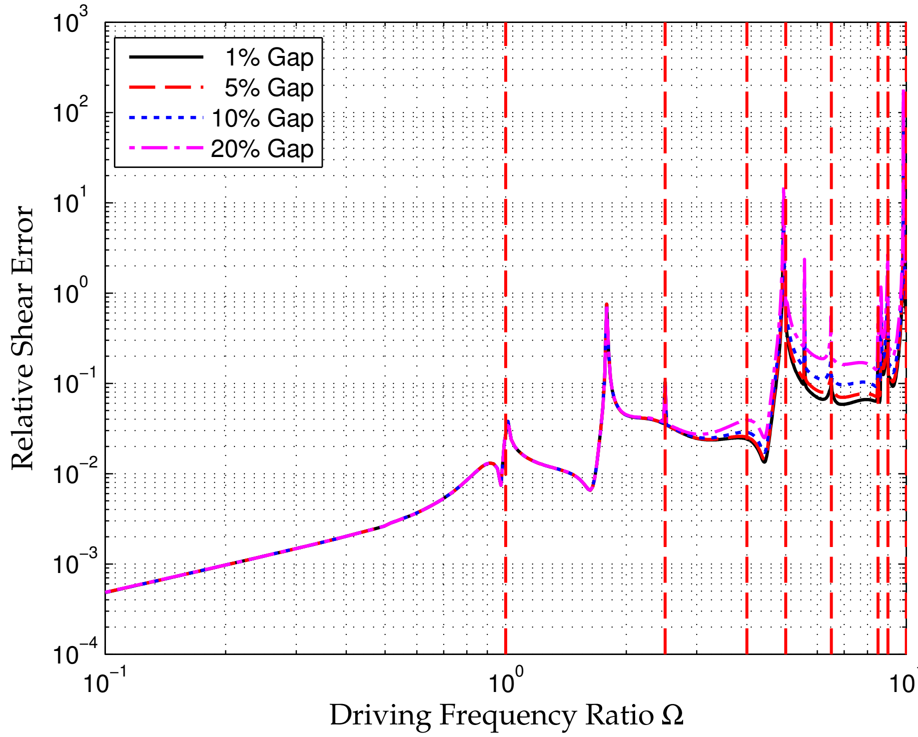

(d) Relative shear error

Figure 3.9 (Cont.): Frequency dependent gaps with $\delta_k = 0.01$ in displacement, rotation, bending moment, and shear.

3.5 Spatial Distribution of Errors

The norms introduced in Section 3.2 are useful for quantifying the overall behavior of the plate when a mismatch is introduced between the domains in the context of hybrid simulation. Given that the local behavior is often a driving factor, it is thus instructive to study the spatial distribution of the errors when imperfect conditions are introduced.

With the solutions presented in Section 2.4, it is relatively straightforward to compute the distribution of the error in space and time. Figures 3.10 and 3.11 demonstrate the absolute difference between the full solution and the hybrid solution with a driving frequency $\Omega = 0.5$ at the time of maximum displacement. The location of the domain separation is indicated with a dashed line. Figures 3.12 and 3.13 show the same results at a higher driving frequency $\Omega = 2$. In both cases a gap is introduced in displacement, rotation, bending moment, and shear at a magnitude of 5% and $\delta_k = 0.01$. Consistent with the derivation in Section 2.4, the edge bending moment is applied at $\eta = 1$. As observed, the general trend is for the error to accumulate around the interface where the gap is introduced. The error seems to propagate to the driving edge as well as the opposite edge for the rotation and the shear, with more propagation seen at the higher frequency. Finally, the peaks of the deformed shape also show some error.

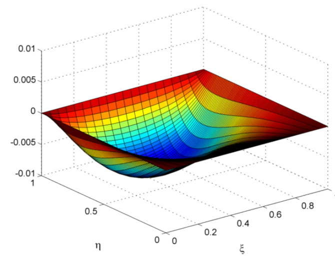

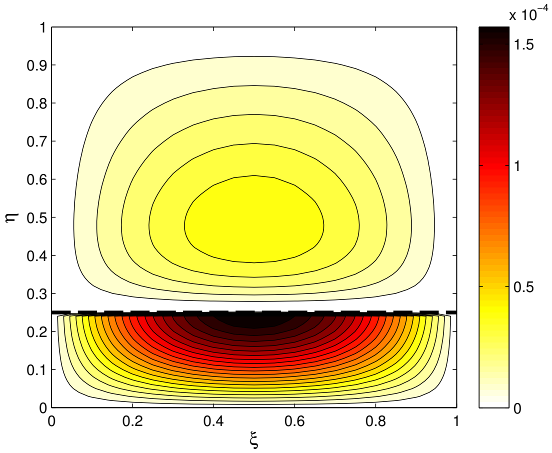

(a) Displacement error

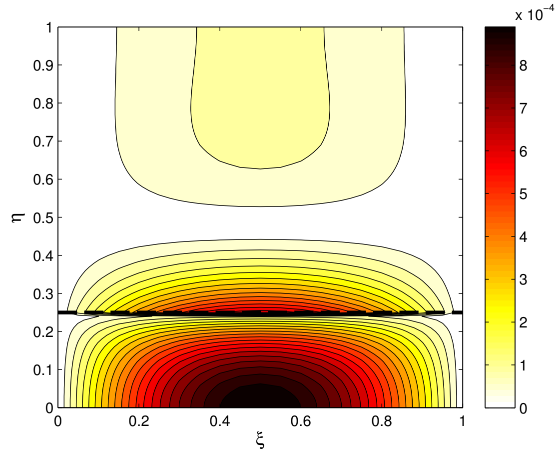

(b) Rotation error

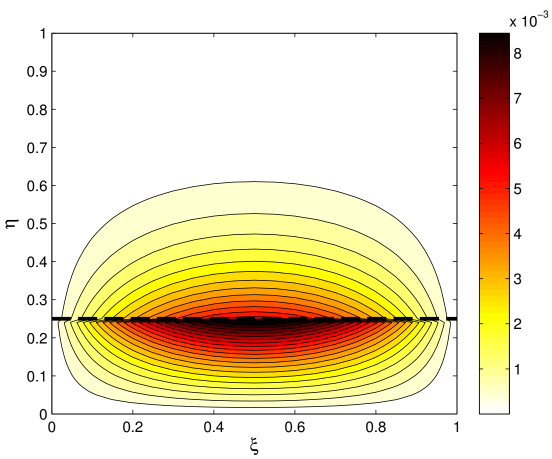

(c) Bending moment error

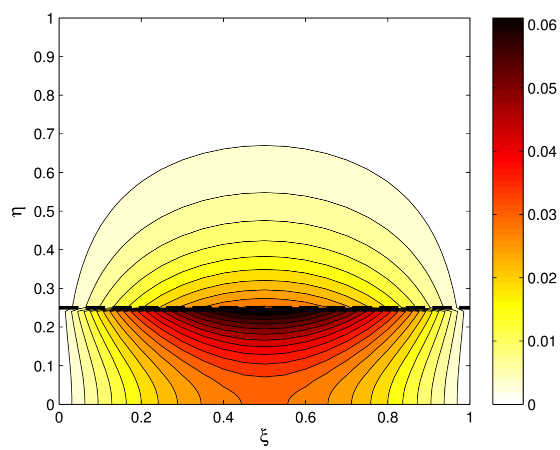

(d) Shear error

Figure 3.10: Contour plot of absolute error in plate at $\Omega = 0.5$ with 5% gap in all quantities and $\delta_k = 0.01$ ($\eta_p = 0.25$).

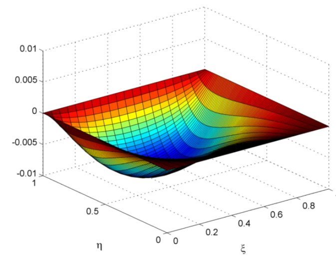

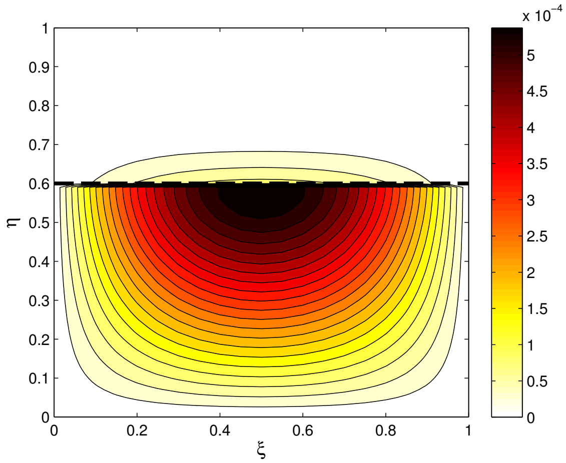

(a) Displacement error

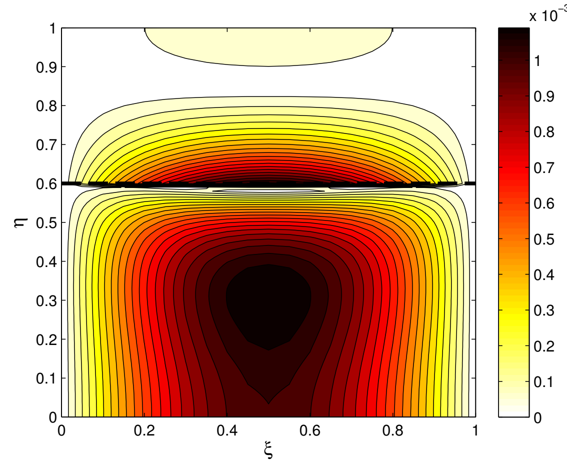

(b) Rotation error

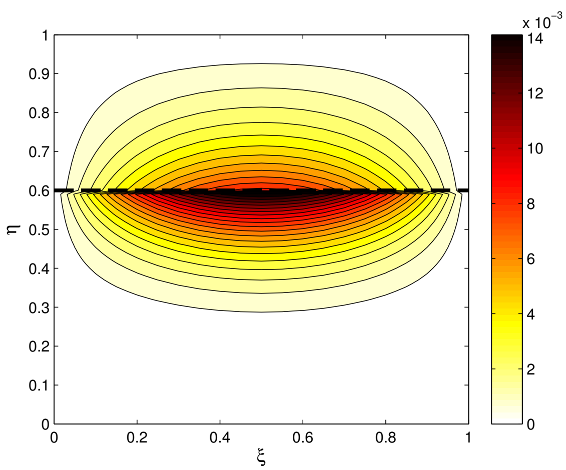

(c) Bending moment error

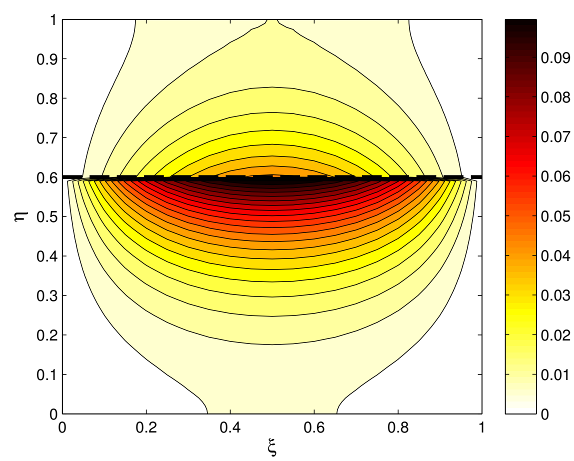

(d) Shear error

Figure 3.11: Contour plot of absolute error in plate at $\Omega = 0.5$ with 5% gap in all quantities and $\delta_k = 0.01$ ($\eta_p = 0.6$).

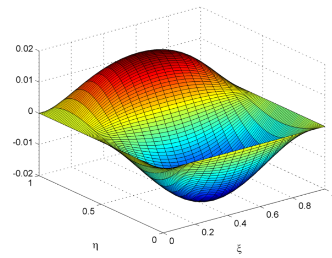

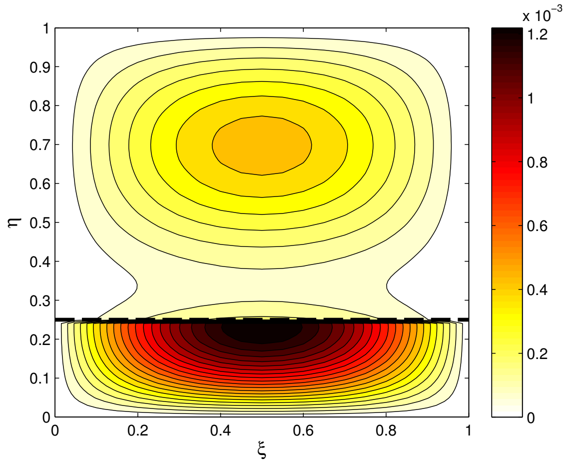

(a) Displacement error

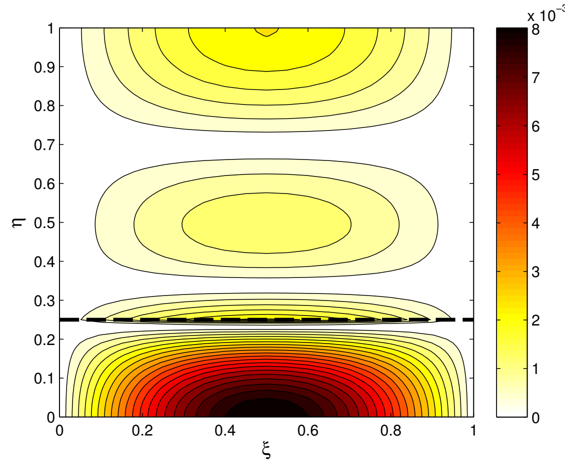

(b) Rotation error

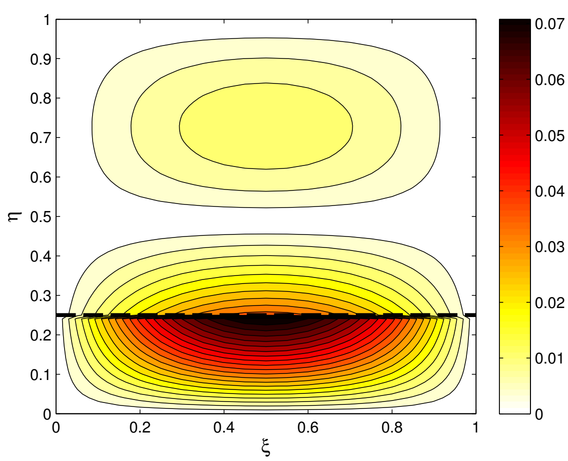

(c) Bending moment error

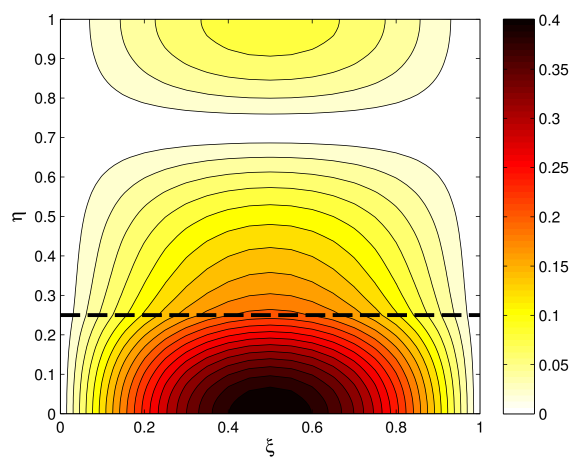

(d) Shear error

Figure 3.12: Contour plot of absolute error in plate at $\Omega = 2$ with 5% gap in all quantities and $\delta_k = 0.01$ ($\eta_p = 0.25$).

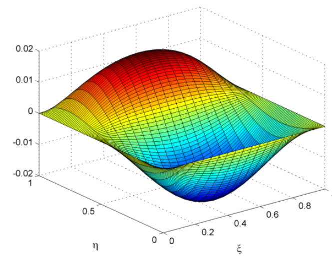

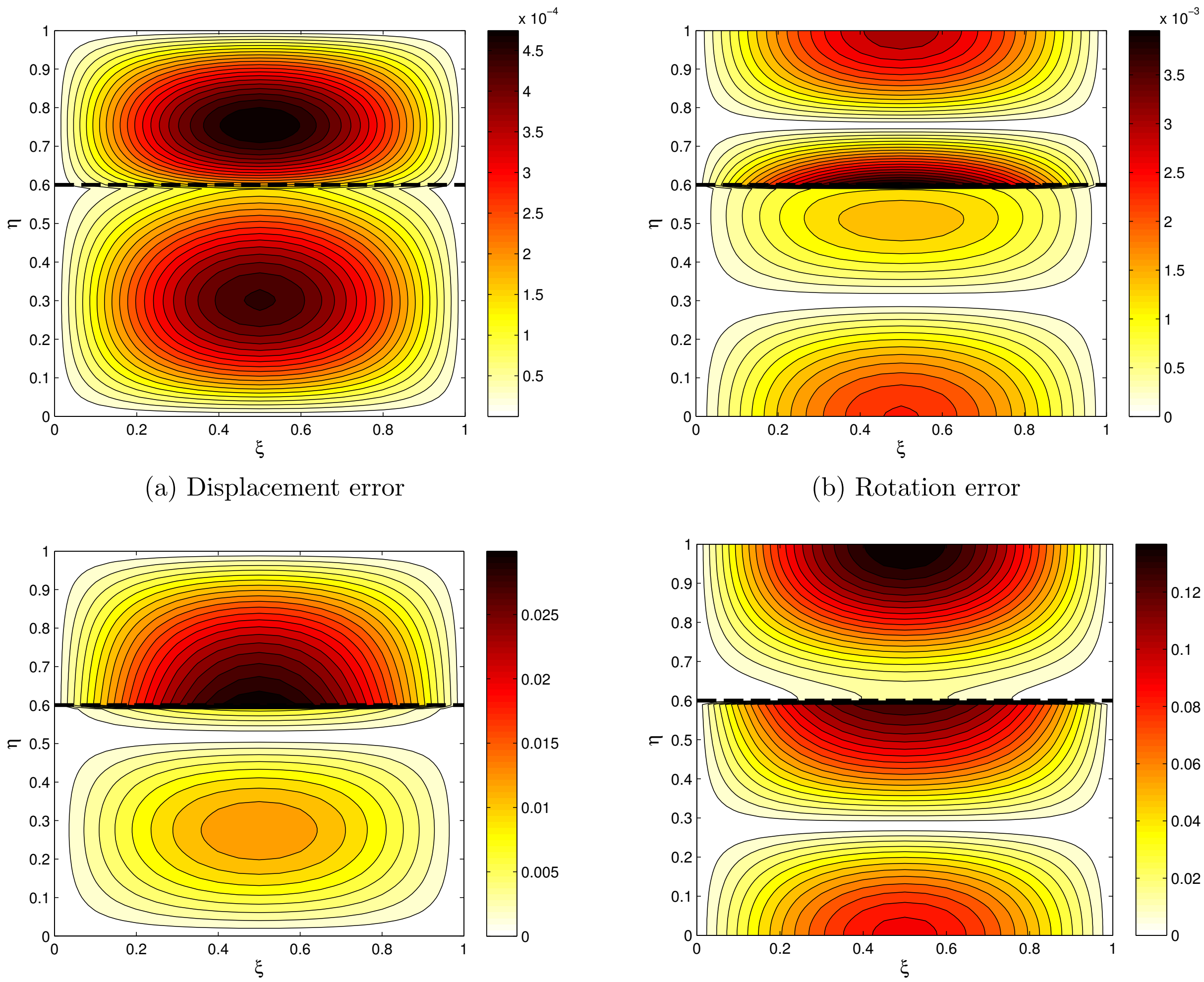

(a) Displacement error

(b) Rotation error

(c) Bending moment error

(d) Shear error

Figure 3.13: Contour plot of absolute error in plate at $\Omega = 2$ with 5% gap in all quantities and $\delta_k = 0.01$ ($\eta_p = 0.6$).

3.6 Excitation of Substructures

The previous results indicated certain discrete frequencies that resulted in larger errors. A careful study of these errors shows that they correspond to natural frequencies of one of the sub-plates of the $\mathcal{P}$ or $\mathcal{C}$-domain. For each domain, the sub-plate is simply, supported on three sides with imposed displacements and rotations on the fourth side or, in other words, clamped on the fourth side. The natural frequencies can be easily computed [Leissa 1973] given the aspect ratios defined by the separation location η_p. Figure 3.14 confirms that for a driving frequency of $\Omega = 1.79$, error spikes only occur at $\eta_p = 0.75$ and again at $\eta_p = 1 - 0.75$, where in each case one of the sub-plates is at the aspect ratio with a natural frequency corresponding to the driving frequency.

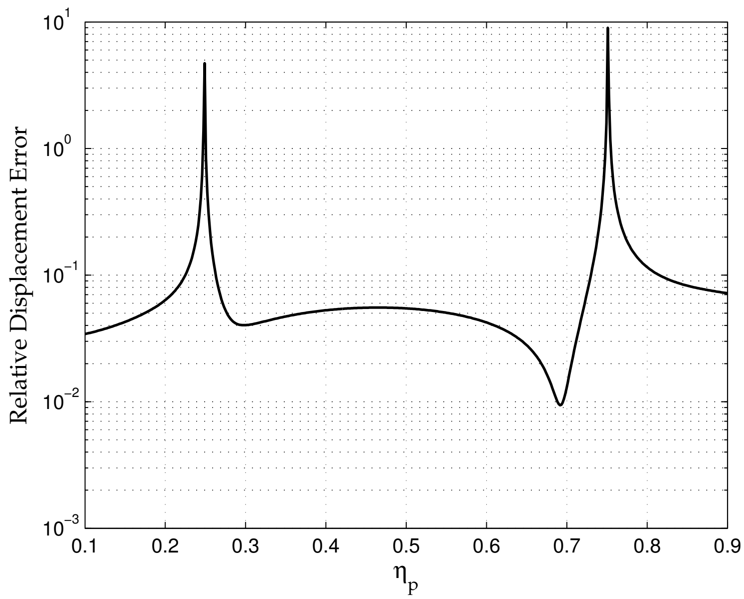

Figure 3.14: Effect of separation location with errors at $\Omega = 1.79$.

A look at the deformation of the hybrid plate with imperfect conditions, shown in Figure 3.15, indicates that the excited $\mathcal{P}$-domain is vibrating with a different mode shape than the fully simply supported (non-hybrid) plate and at a higher amplitude. Although the solution would be expected to be unbounded at the natural frequencies, because the sub-plates are being driven by kinematic quantities (i.e., displacements and rotations), the solution remains bounded.

As shown in Figure 3.1, these frequencies are not excited when no error is imposed. This is consistent with the hybrid formulation, which recovers the solution of the full simply supported plate when there is no gap. Figure 3.5a indicates that when only displacement and rotation errors of equivalent magnitudes are present, these frequencies are not excited.

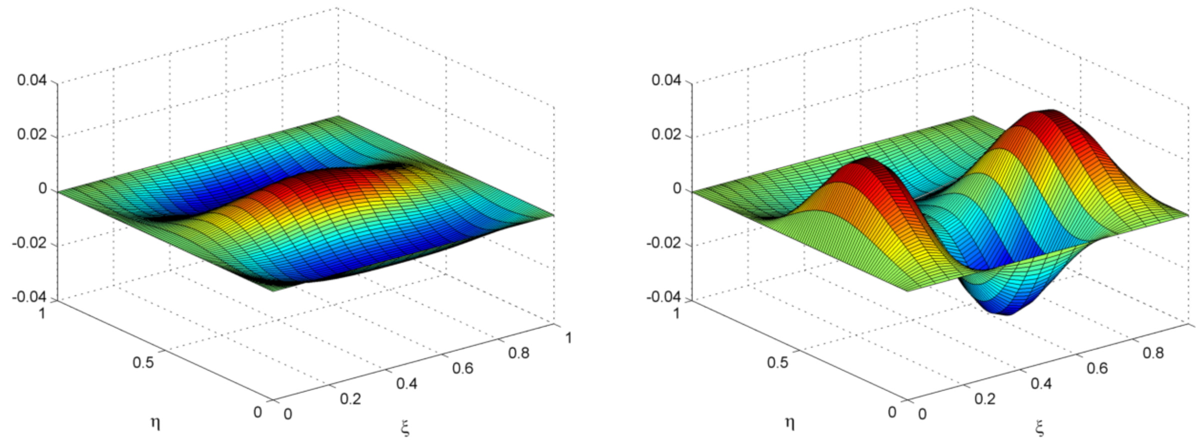

(a) Zero errors

(b) Imposed errors

Figure 3.15: Deflected shape of a plate at $\Omega = 5.58$ with $\eta_p = 0.75$. The $\mathcal{P}$-domain is seen to vibrate at its natural frequency.

3.7 Discussion of Results

The preceding results leads to several conclusions. Note that the following discussion is based primarily on the results of the analysis of an undamped, elastic homogeneous isotropic Kirchhoff-Love plate under infinitesimal kinematics and the Bernoulli assumptions of "plane sections remain plane." Furthermore, the plate is subjected to harmonic excitation, which plays an important role in engineering applications in the study of vibrations and other phenomena; hybrid testing applications have generally been conducted with transient excitation. Results were corroborated with hybrid formulations of a rod under axial loading and an Euler-Bernoulli beam in flexure by the work of Drazin [Drazin 2013]. Generalization of the results to hybrid simulation and pseudodynamic testing is not possible without considerably more study in an ongoing effort.

3.7.1 Effect of Excitation Frequency

The first and most apparent results observed in Sections 3.3.2 and 3.4 is the relatively large error at driving frequencies larger than the fundamental frequency. Below the fundamental frequency, the error for the most part is well-behaved being log-linear or almost constant as the fundamental frequency of the system is approached and beyond, however, the errors become highly unpredictable. The implications of this could mean that hybrid testing may not be reliable at high frequencies, which is certainly observed with ground motion excitation seen in earthquake engineering applications; *however*, the effect of damping is not included in this presentation. Damping plays a significant role in the dynamical response of systems, and it is necessary to include these effects before a more formal conclusion can be drawn.

It has been noted that hybrid simulation and pseudodynamic testing produce more favorable results in earthquake engineering applications for systems that exhibit inelastic response than corresponding elastic systems [Chang et al. 2011]. A structural system that undergoes inelastic deformation due to yielding exhibits significantly higher effective damping than the corresponding elastic system, where equivalent viscous damping is observed at about 2 to 5% of critical damping for typical structural systems [Chopra 2004]. The less favorable response of the lightly damped elastic systems subjected to the high-frequency excitation of an earthquake ground acceleration history is consistent with the conclusions of the theoretical study of the plate; however, it is necessary to include the effect of damping to complete this argument.

Also observed is the tendency to accumulate significant errors around the natural frequencies. This result has been presented as a conclusion of previous studies [Shing and Mahin 1983]. That work also concluded that with the presence of a discrete computational substructure utilizing a numerical integration strategy to solve the equations of motion [Newmark 1959] in a pseudodynamic setting, the error is proportional to $\bar{\omega}\Delta t$, where $\bar{\omega}$ is a natural frequency of the system and Δt is the time step of the numerical integration. It is not necessarily appropriate to consider that result in this context; however, it is also observed here that there are larger errors at the higher frequencies of the system.

3.7.2 Effect of Error Magnitudes

It is observed that the slightest introduction of error leads to a quick increase of the global error in the system relative to the perfect case. Further increase of error has a lesser effect on the global response. The implication of this is that significant efforts to improve the experimental set-up may not have a significant impact on the overall response. Because there will always be some error in the system due to the nature of the hybrid testing, it may not be particularly advantageous to expend continued effort to improve the set-up. That said, simple error compensation techniques maybe worth exploring [Elkhoraibi and Mosalam 2007].

3.7.3 Impact of Time Delay

The results presented in Section 3.3.4 indicate that the phase of the error plays a larger role than the magnitude. Physically speaking, a system that is out-of-phase exhibits larger errors than corresponding in-phase systems. This is an expected result granted that a time delay will cause an accumulation of error with increasing time. The implication is that accurate control of the physical substructure in hybrid simulation is critical for accurate results [Ahmadizadeh et al. 2008].

3.7.4 Excitation of Substructures

Several discrete frequencies not being natural frequencies of the system exhibit a relatively large accumulation of error. A careful study of these frequencies indicated that the substructures are being excited when there is error between the domains. The implication of this is that the individual substructures can be excited independently during a hybrid test, particularly when the excitation is transient. This is consistent with studies that have demonstrated that delay in the control can lead to excitation of higher modes of the physical substructure [Shing and Mahin 1987].

This behavior was observed in experiments carried out in an earlier phase of this project when the effect of real-time hybrid simulation with large computational substructures was investigated, which is discussed briefly in Appendix D. In this case, components of the experimental set-up (the hydraulic oil-column in the actuator system) were observed to be excited [Mosalam et al. 2012a]. Although not intended as part of the physical substructure, the entire experimental set-up inevitably becomes part of the physical substructure, and in this case is excited, resulting in significant errors. Furthermore, when a different computational model is used, a different mode of the physical substructure is seen to be excited, leading to some errors (Figure D.3).

3.7.5 Propagation of Errors

The error introduced as a mismatch at the interface does not remain localized at this location. In certain cases, especially at higher driving frequencies, error is seen to spread. Error is observed at the peaks of the system, indicating that the peak global response is affected by local introduction of errors. Furthermore, depending on the boundary conditions, static and kinematic quantities at supports may also exhibit significant errors. This can play an important role as support reactions are of great interest in stress analysis.

4. Conclusion

4.1 Summary

Hybrid simulation has the potential to solve many of today's challenging problems in science and engineering by overcoming the limitations of traditional experimentation and analysis techniques. But like all methods, it faces unique limitations that are currently being addressed to insure robust and effective applicability. One of the primary drawbacks is the lack of a well-established theory. The results presented here are the first in a continuing endeavor to investigate hybrid simulation and pseudodynamic testing in a theoretical context and provide error bounds.

Beginning with the abstract problem, hybrid simulation was presented as a theoretical problem. It was then applied to an important and prevalent problem in mechanics: dynamic response of plates. Beginning with Kirchhoff-Love thin plate theory, "hybrid" equations were presented for a mathematically split domain representing the physical and computational substructures of hybrid simulation. Typical of hybrid testing, excitation was provided in the computational domain, and the physical domain was constrained to match the response at the interface. The hybrid solution was shown to match the non-hybrid plate within a thoroughly presented precision of numerical evaluation in the absence of introduced error. Error was subsequently introduced between the domains and its effect carefully studied.

The following conclusions were made as a result of this study

1. Without the presence of damping, significant errors are seen at driving frequencies near and above the fundamental frequency.

2. There is a tendency to accumulate errors in the vicinity of the natural frequencies. This has been observed experimentally in the context of pseudodynamic testing by others.

3. Systems with out-of-phase response of the physical and computational substructures exhibit larger errors than corresponding in-phase systems. This emphasizes the need for accurate control and delay compensation.

4. There is a tendency for the error to propagate away from the interface of the physical and computational substructure at higher frequencies, affecting both peak and boundary responses.

5. Under the presence of domain mismatch, natural frequencies of the substructures can be excited and lead to relatively large errors. This was observed in experiments per-

formed in an earlier effort to study the effects of numerically intensive computational substructures in real-time hybrid simulation.

4.2 Ongoing Studies and Concluding Remarks

The continued study of the theoretical development of hybrid simulation should involve the following:

1. The inclusion of damping, which plays an important role in the dynamical response of systems; its inclusion is critical to generalize the results presented here.

2. More robust error models as those presented here were of the form of a time delay with a dependence on frequency intended to simulate the errors due to experimental control in hybrid testing. Many other forms of errors have been noted and studied, and should be investigated in the context of the theoretical framework.

3. Extension of concepts to (a) slower than real-time and (b) faster than real-time hybrid simulation.

4. More realistic mathematical theory as the results presented have only been for the simplest case of linear elasticity, isotropy, infinitesimal kinematics, and negligible through-thickness deformation. Most of the observed physical response, in particular the problems of greatest interest, involve large deformation kinematics, material nonlinearity, anisotropy, and inhomogeneity.

5. Extension of concepts beyond solid mechanics as some of the most challenging problems of importance are in fluid dynamics, heat flow, multi-physics problems, and more.

Hybrid simulation has the potential to solve many of today's most challenging problems in engineering and provide a powerful means to face the challenges of tomorrow. A theoretical framework for the technique is needed to achieve a more robust implementation across multiple disciplines. The study presented herein should only be the beginning of a continued effort on the theoretical development of hybrid simulation.

Bibliography

Ahmadizadeh, M., G. Mosqueda, and A. M Reinhorn (2008). "Compensation of actuator delay and dynamics for real time hybrid structural simulation". In: *Earthquake Engineering and Structural Dynamics* 37, pp. 21–42.

Campbell, S. and B. Stojadinovic (1998). "A system for simultaneous pseudodynamic testing of multiple substructures". In: *Proceedings, Sixth U.S. National Conference on Earthquake Engineering*. Seattle, WA.

Chang, S., Y. Yang, and C. Hsu (2011). "A family of explicit algorithms for general pseudodynamic testing". In: *Earthquake Engineering and Engineering Vibration* 10, pp. 51–56.

Chopra, A. K. (2004). *Dynamics of Structures: Theory and Applications to Earthquake Engineering*. Upper Saddle River, NJ: Prentice Hall.

Combescure, D. and P. Pegon (1997). "Alpha-operator splitting time integration technique for pseudodynamic testing error propagation analysis". In: *Soil Dynamics and Earthquake Engineering* 16.7-8, pp. 427–443.

Conte, J. P. and T. L. Trombetti (2000). "Linear dynamic modeling of a uni-axial shaking table system". In: *Earthquake Engineering and Structural Dynamics* 29, pp. 1375–1404.

Dermitzakis, S. N. and S. A. Mahin (1985). Development of substructuring techniques for on-line computer controlled seismic performance testing, *Report No. UCB/EERC-84/04*, Earthquake Engineering Research Center, University of California, Berkeley.

Drazin, P. (2013). "*Hybrid Simulation Theory Featuring Bars and Beams*". M.S. Report. Department of Mechanical Engineering, University of California, Berkeley.

Elkhoraibi, T. and K. M. Mosalam (2007). Generalized hybrid simulation framework for structural systems subjected to seismic loading, *PEER Report 2007/101*, Pacific Earthquake Research Center, University of California, Berkeley.

Gorman, D. J. and R.K. Sharma (1976). "A comprehensive approach to the free vibration analysis of rectangular plates by use of the method of superposition". In: *Journal of Sound and Vibration* 47, pp. 126–128.

Govindjee, S. (2012). *Engineering Mechanics of Deformable Solids: A Presentation with Exercises*. USA: Oxford University Press; 1st Edition.

Graff, K. F. (1975). *Wave Motion In Elastic Solids*. London: Oxford University Press.

Horiuchi, T. et al. (1999). "Real-time hybrid experimental system with actuator delay compensation and its application to a piping system with energy absorber". In: *Earthquake Engineering and Structural Dynamics* 28.10, pp. 1121–1141.

Igarashi, A., F. Seible, and G. A. Hegemeier (1993). “Development of the pseudodynamic technique for testing a full scale 5-story shear wall structure”. In: *U.S. - Japan Seminar, Development and Future Dimensions of Structural Testing Techniques*. Honolulu, HI.

Kronrod, A. S. (1965). *Nodes and weights of quadrature formulas: Sixteen-place tables*. Consultants Bureau New York.

Leissa, A. W. (1969). *Vibration of Plates*. Acoustical Society of America.

Leissa, A. W. (1973). “The free vibration of rectangular plates”. In: *Journal of Sound and Vibration* 31, pp. 257–293.

MATLAB (2013). *MATLAB*. Mathworks. URL: `http://www.mathworks.com`.

Mosalam, K. M. and M. S. Günay (2013). “Hybrid Simulations: Theory, Applications, and Future Directions”. In: *Advanced Materials Research*, pp. 67–95.

Mosalam, K. M. et al. (2012a). “EAGER: Next Generation Hybrid Simulation: Theory, Evaluation, and Development”. In: *Poster for the NSF Engineering Research and Innovation Conference and Mechanical and Manufacturing Innovation (CMMI) Grantee Conference*. Boston, MA.

Mosalam, K. M. et al. (2012b). *Seismic Performance of Substation Insulator Posts for Vertical-Break Disconnect Switches*. Tech. rep. California Energy Commission.

Mosqueda, G. (2003). “Continuous hybrid simulation with geographically distributed substructures”. PhD thesis. University of California, Berkeley. 232 pp.

Nakashima, M. (2001). “Development, potential, and limitations of real-time online (pseudodynamic) testing”. In: *Philosophical Transactions of the Royal Society: Mathematical, Physical and Engineering Sciences* 359, pp. 1851–1867.

nees@berkeley (2013). *nees@berkeley*. George E. Brown Jr. Network for Earthquake Engineering Simulation (NEES). URL: `http://nees.berkeley.edu`.

Newmark, N. M. (1959). “A method of computation for structural dynamics”. In: *Journal of Engineering Mechanics, ASCE* 67.

OpenFresco (2013). *Open Framework for Experimental Setup and Control*. URL: `http://openfresco.neesforge.nees.org`.

OpenSEES (2013). *Open System for Earthquake Engineering Simulation*. URL: `http://opensees.berkeley.edu`.

Richards, F. J. (1959). “A flexible growth function for empirical use”. In: *Journal of Experimental Botany* 10, pp. 290–300.

Schellenberg, A. H. (2008). “*Advanced Implementation of Hybrid Simulation*”. PhD thesis. Department of Civil and Environmental Engineering, University of California, Berkeley. 348 pp.

Shing, P. S. B. and S. A. Mahin (1983). Experimental error propagation in pseudodynamic testing, *Report No. UCB/EERC-83/12*, Earthquake Engineering Research Center, University of California, Berkeley.

Shing, P. S. B. and S. A. Mahin (1987). “Elimination of spurious higher-mode response in pseudodynamic tests”. In: *Earthquake Engineering and Structural Dynamics* 15, pp. 409–424.

Strang, G. (2005). *Linear Algebra and its Applications*. Cengage Learning; 4th Edition.

Szilard, R. (2004). *Theories and Applications of Plate Analysis*. Hoboken, NJ: John Wiley & Sons.

Takanashi, K. and M. Nakashima (1987). "Japanese activities on on-line testing". In: *Journal of Engineering Mechanics* 113, pp. 1014–1032.

Takanashi, K. et al. (1975). "Nonlinear earthquake response analysis of structures by a computer-actuator on-line system". In: *Bulletin of Earthquake Resistant Structure Research Center* 8, pp. 1–17.

Taylor, R. L. and S. Govindjee (2004). "Solution of clamped rectangular plate problems". In: *Communications in Numerical Methods in Engineering* 20, pp. 757–765.

Thewalt, C. R. and S. A. Mahin (1987). *Hybrid solution techniques for generalized pseudo-dynamic testing*. Tech. rep. Berkeley, CA: Earthquake Engineering Research Center.

Timoshenko, S. (1959). *Theory of Plates and Shells*. Blacklick, OH: McGraw-Hill College; 2nd Edition.

Appendix A

Plate Notation

The various plate quantities used throughout the thesis are presented below. Figure A.1 shows a differential plate element with the consistent sign convention [Graff 1975].

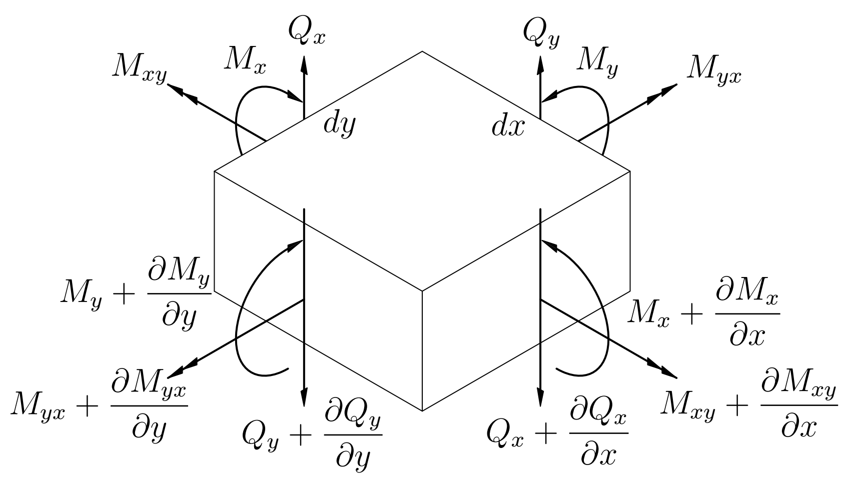

Figure A.1: Differential plate element.

It follows that the shears per unit length are

$$Q_x = \frac{\partial M_x}{\partial x} + \frac{\partial M_{yx}}{\partial y}, \tag{A.1a}$$

$$Q_y = \frac{\partial M_y}{\partial y} - \frac{\partial M_{xy}}{\partial x}. \tag{A.1b}$$

Note that the total shear also has a contribution from the twisting moment as shown by Kirchhoff [Timoshenko 1959], as seen in Equation (A.6). Given the Euler-Bernoulli assumptions of "plane sections remain plane," the strains can be defined as

$$\varepsilon_x = -z\frac{\partial^2 w}{\partial x^2} \quad \varepsilon_y = -z\frac{\partial^2 w}{\partial y^2} \quad \gamma_y = -2z\frac{\partial^2 w}{\partial x \partial y}, \tag{A.2}$$

where the engineering shear strain is used. For an isotropic elastic material, the stress is given by Hooke's law:

$$\begin{pmatrix} \sigma_x \\ \sigma_y \\ \tau_{xy} \end{pmatrix} = \frac{E}{(1+\nu)(1-2\nu)} \begin{pmatrix} 1-\nu & \nu & 0 \\ \nu & 1-\nu & 0 \\ 0 & 0 & \frac{1-2\nu}{2} \end{pmatrix} \begin{pmatrix} \varepsilon_x \\ \varepsilon_y \\ \gamma_{xy} \end{pmatrix}. \tag{A.3}$$

With the center-plane of the differential element as reference, the moments per unit length are defined as

$$M_x = \int_{-h/2}^{h/2} z\sigma_x dz \quad M_y = \int_{-h/2}^{h/2} z\sigma_y dz \quad M_{xy} = -\int_{-h/2}^{h/2} z\tau_{xy} dz, \tag{A.4}$$

which leads to

$$M_x = -D(\frac{\partial^2 w}{\partial x^2} + \nu \frac{\partial^2 w}{\partial y^2}), \tag{A.5a}$$

$$M_y = -D(\frac{\partial^2 w}{\partial y^2} + \nu \frac{\partial^2 w}{\partial x^2}), \tag{A.5b}$$

$$M_{xy} = D(1-\nu)\frac{\partial^2 w}{\partial x \partial y}, \tag{A.5c}$$

where the D is given by Equation (2.10). The total shears are

$$V_x = Q_x - \frac{\partial M_{xy}}{\partial y}, \tag{A.6a}$$

$$V_y = Q_y - \frac{\partial M_{yx}}{\partial x}. \tag{A.6b}$$

The contributions of the shears from the shear stress are

$$Q_x = -D(\frac{\partial^3 w}{\partial x^3} + \frac{\partial^3 w}{\partial x \partial y^2}), \tag{A.7a}$$

$$Q_y = -D(\frac{\partial^3 w}{\partial y^3} + \frac{\partial^3 w}{\partial x^2 \partial y}). \tag{A.7b}$$

And the total shears are

$$V_x = -D(\frac{\partial^3 w}{\partial x^3} + (1-2\nu)\frac{\partial^3 w}{\partial x \partial y^2}), \tag{A.8a}$$

$$V_y = -D(\frac{\partial^3 w}{\partial y^3} + (1-2\nu)\frac{\partial^3 w}{\partial x^2 \partial y}). \tag{A.8b}$$

Finally the governing equation of motion is given by Equation (2.9).

Appendix B

Coefficients of Joining System

The system of algebraic equations given by Equation (2.36) is to be solved to determine the gap functions at the interface. The coefficients of this system are given below.

For $\alpha^4 < \beta^4$

$$M_1 = [{\hat{\gamma}_2}^2 \gamma_1 \cosh(\gamma_1 b_1) \sin(\gamma_2 b_1) - {\hat{\gamma}_1}^2 \gamma_2 \sinh(\gamma_1 b_1) \cos(\gamma_2 b_1)]/R_1, \tag{B.1a}$$

$$M_2 = [{\hat{\gamma}_1}^2 \gamma_2 \sinh(\gamma_1 b_2) \cos(\gamma_2 b_2) - {\hat{\gamma}_2}^2 \gamma_1 \cosh(\gamma_1 b_2) \sin(\gamma_2 b_2)]/R_2, \tag{B.1b}$$

$$M_3 = [({\hat{\gamma}_1}^2 - {\hat{\gamma}_2}^2) \sinh(\gamma_1 b_1) \sin(\gamma_2 b_1)]/R_1, \tag{B.1c}$$

$$M_4 = [({\hat{\gamma}_1}^2 - {\hat{\gamma}_2}^2) \sinh(\gamma_1 b_2) \sin(\gamma_2 b_2)]/R_2, \tag{B.1d}$$

$$M_5 = w_0 \left[{\hat{\gamma}_2}^2 \cos(\gamma_2 b_2) - {\hat{\gamma}_1}^2 \cosh(\gamma_1 b_2) + \frac{{\hat{\gamma}_1}^2 \sinh(\gamma_1 b_2)(\gamma_2 + P_1) + {\hat{\gamma}_2}^2 \sin(\gamma_2 b_2)(\gamma_1 - P_2)}{R_2} \right], \tag{B.1e}$$

$$V_1 = [({\hat{\gamma}_2}^3 \gamma_1 - {\hat{\gamma}_1}^3 \gamma_2) \cosh(\gamma_1 b_1) \cos(\gamma_2 b_1)]/R_1, \tag{B.1f}$$

$$V_2 = [({\hat{\gamma}_2}^3 \gamma_1 - {\hat{\gamma}_1}^3 \gamma_2) \cosh(\gamma_1 b_2) \cos(\gamma_2 b_2)]/R_2, \tag{B.1g}$$

$$V_3 = [{\hat{\gamma}_1}^3 \cosh(\gamma_1 b_1) \sin(\gamma_2 b_1) - {\hat{\gamma}_2}^3 \sinh(\gamma_1 b_1) \cos(\gamma_2 b_1)]/R_1, \tag{B.1h}$$

$$V_4 = [{\hat{\gamma}_2}^3 \sinh(\gamma_1 b_2) \cos(\gamma_2 b_2) - {\hat{\gamma}_1}^3 \cosh(\gamma_1 b_2) \sin(\gamma_2 b_2)]/R_2, \tag{B.1i}$$

$$V_5 = w_0 \left[{\hat{\gamma}_1}^3 \sinh(\gamma_2 b_2) + {\hat{\gamma}_2}^3 \sin(\gamma_2 b_2) - \frac{{\hat{\gamma}_1}^3 \cosh(\gamma_1 b_2)(\gamma_2 + P_1) + {\hat{\gamma}_2}^3 \cos(\gamma_2 b_2)(\gamma_1 - P_2)}{R_2} \right]. \tag{B.1j}$$

The following terms, related to the mixed derivatives of the moments and shears (see Appendix A) were introduced for convenience:

$$\begin{array}{ll} {\hat{\gamma}_1}^2 = \gamma_1^2 - \nu\alpha^2 & {\hat{\gamma}_2}^2 = -\gamma_2^2 - \nu\alpha^2, \\ {\hat{\gamma}_1}^3 = \gamma_1^3 - (1-2\nu)\alpha^2\gamma_1 & {\hat{\gamma}_2}^3 = -\gamma_2^3 - (1-2\nu)\alpha^2\gamma_2 \end{array} \tag{B.2}$$

For $\alpha^4 > \beta^4$

$$M_1 = [\hat{\gamma_1}^2 \gamma_2' \cosh(\gamma_1 b_1) \sinh(\gamma_2' b_1) - \hat{\gamma_2'}^2 \gamma_1 \sinh(\gamma_1 b_1) \cosh(\gamma_2' b_1)]/R_1^*, \tag{B.3a}$$

$$M_2 = [\hat{\gamma_1}^2 \gamma_2' \sinh(\gamma_1 b_2) \cosh(\gamma_2' b_2) - \hat{\gamma_2'}^2 \gamma_1 \cosh(\gamma_1 b_2) \sinh(\gamma_2' b_2)]/R_2^*, \tag{B.3b}$$

$$M_3 = [(\hat{\gamma_2'}^2 - \hat{\gamma_1}^2) \sinh(\gamma_1 b_1) \sinh(\gamma_2' b_1)]/R_1^*, \tag{B.3c}$$

$$M_4 = [(\hat{\gamma_2'}^2 - \hat{\gamma_1}^2) \sinh(\gamma_1 b_2) \sinh(\gamma_2' b_2)]/R_2^*, \tag{B.3d}$$

$$M_5 = w_0^* \left[\hat{\gamma_2'}^2 \cosh(\gamma_2' b_2) - \hat{\gamma_1}^2 \cosh(\gamma_1 b_2) - \frac{\hat{\gamma_1}^2 \sinh(\gamma_1 b_2)(\gamma_2' + P_1^*) + \hat{\gamma_2}^2 \sinh \gamma_2' b_2 (\gamma_1 - P_2^*)}{R_2^*} \right], \tag{B.3e}$$

$$V_1 = [(\hat{\gamma_1}^3 \gamma_2' - \hat{\gamma_2'}^3 \gamma_1) \cosh(\gamma_1 b_1) \cosh(\gamma_2' b_1)]/R_1^*, \tag{B.3f}$$

$$V_2 = [(\hat{\gamma_1}^3 \gamma_2' - \hat{\gamma_2'}^3 \gamma_1) \cosh(\gamma_1 b_2) \cosh(\gamma_2' b_2)]/R_2^*, \tag{B.3g}$$

$$V_3 = [\hat{\gamma_2'}^3 \sinh(\gamma_1 b_1) \cosh(\gamma_2' b_1) - \hat{\gamma_1}^3 \cosh(\gamma_1 b_1) \sinh(\gamma_2' b_1)]/R_1^*, \tag{B.3h}$$

$$V_4 = [\hat{\gamma_1}^3 \cosh(\gamma_1 b_2) \sinh(\gamma_2' b_2) - \hat{\gamma_2'}^3 \sinh(\gamma_1 b_2) \cosh(\gamma_2' b_2)]/R_2^*, \tag{B.3i}$$

$$V_5 = w_0^* \left[\hat{\gamma_1}^3 \sinh(\gamma_2' b_2) - \hat{\gamma_2'}^3 \sinh(\gamma_2' b_2) + \frac{\hat{\gamma_1}^3 \cosh(\gamma_1 b_2)(\gamma_2' + P_1^*) + \hat{\gamma_2'}^3 \cosh(\gamma_2' b_2)(\gamma_1 - P_2^*)}{R_2^*} \right]. \tag{B.3j}$$

Where $\gamma_2' = -\gamma_2$ is introduced for convenience and

$$\begin{aligned} \hat{\gamma_1}^2 &= \gamma_1^2 - \nu\alpha^2 & \hat{\gamma_2'}^2 &= \gamma_2'^2 - \nu\alpha^2, \\ \hat{\gamma_1}^3 &= \gamma_1^3 - (1-2\nu)\alpha^2\gamma_1 & \hat{\gamma_2'}^3 &= \gamma_2'^3 - (1-2\nu)\alpha^2\gamma_2'. \end{aligned} \tag{B.4}$$

and for $\alpha^4 = \beta^4$

$$M_1 = [-\hat{\gamma_1}^2 \gamma_1 b_1 + (\hat{\gamma_1}^2 - 2\gamma_1^2) \sinh(\gamma_1 b_1) \cosh(\gamma_1 b_1)]/R_1', \tag{B.5a}$$

$$M_2 = [\hat{\gamma_1}^2 \gamma_1 b_2 - (\hat{\gamma_1}^2 - 2\gamma_1^2) \sinh(\gamma_1 b_2) \cosh(\gamma_1 b_1)]/R_2', \tag{B.5b}$$

$$M_3 = [2\gamma_1 \sinh^2(\gamma_1 b_1)]/R_1', \tag{B.5c}$$

$$M_4 = [2\gamma_1 \sinh^2(\gamma_1 b_2)]/R_2', \tag{B.5d}$$

$$M_5 = \begin{array}{c} -w_0' \left[\hat{\gamma_1}^2 b_2 \sinh(\gamma_1 b_2) + 2\gamma_1 \cosh(\gamma_1 b_2) + \dfrac{\hat{\gamma_1}^2 b_2^2 \gamma_1 \sinh(\gamma_1 b_2)}{R_2'} \right. \\ \left. - \dfrac{(\hat{\gamma_1}^2 b_2 \cosh(\gamma_1 b_2) + 2\gamma_1 \sinh(\gamma_1 b_2)) \sinh^2(\gamma_1 b_2)}{R_2'} \right] \end{array}, \tag{B.5e}$$

$$V_1 = -2\gamma_1^3 \cosh^2(\gamma_1 b_1)]/R_1', \tag{B.5f}$$

$$V_2 = -2\gamma_1^3 \cosh^2(\gamma_1 b_2)]/R_2', \tag{B.5g}$$

$$V_3 = [\tilde{\gamma_1}^3 \sinh(\gamma_1 b_1) \cosh(\gamma_1 b_1) - \hat{\gamma_1}^3 b_1]/R_1', \tag{B.5h}$$

$$V_4 = [-\tilde{\gamma_1}^3 \sinh(\gamma_1 b_2) \cosh(\gamma_1 b_2) + \hat{\gamma_1}^3 b_2]/R_2', \tag{B.5i}$$

$$V_5 = \begin{aligned} & w_0' \Bigg[\hat{\gamma_1}^3 b_2 \cosh(\gamma_1 b_2) + \tilde{\gamma_1}^3 \sinh(\gamma_1 b_2) + \frac{\hat{\gamma_1}^3 b_2^2 \gamma_1 \cosh(\gamma_1 b_2)}{R_2'} \\ & \qquad - \frac{(\hat{\gamma_1}^3 b_2 \sinh(\gamma_1 b_2) + \tilde{\gamma_1}^3 \cosh(\gamma_1 b_2)) \sinh^2(\gamma_1 b_2)}{R_2'} \Bigg]. \end{aligned} \tag{B.5j}$$

$$\begin{aligned} & \hat{\gamma_1}^2 = \gamma_1^2 - \nu\alpha^2 && , \\ & \hat{\gamma_1}^3 = \gamma_1^3 - (1-2\nu)\alpha^2\gamma_1 && \tilde{\gamma_1}^3 = 3\gamma_1^2 - (1-2\nu)\alpha^2. \end{aligned} \tag{B.6}$$

Appendix C

Integration of the Error Norms

The terms of the integrand in Equation (3.45) involve the product of two infinite series. For the purposes of this integration, finite series with a sufficient number of terms for a required accuracy will be used. The objective is to compute the following integral:

$$\int_\tau \int_\xi \int_\eta \left(\sum_{m=1,3,...}^{M} a_m(\xi, \eta, \tau) \right) \left(\sum_{n=1,3,...}^{N} b_n(\xi, \eta, \tau) \right) \, d\eta \, d\xi \, d\tau. \tag{C.1}$$

where

$$a_m(\xi, \eta, \tau) = X_{ma}(\xi) Y_{ma}(\eta) T_a(\tau). \tag{C.2}$$

$$b_n(\xi, \eta, \tau) = X_{nb}(\xi) Y_{nb}(\eta) T_b(\tau). \tag{C.3}$$

Equation (C.1) can be expressed as

$$\begin{aligned} &\int_\tau \int_\xi \int_\eta [a_1 b_1 + a_1 b_2 + a_2 b_1 + ... + a_2 b_N + ... + a_M b_N] \, d\eta \, d\xi \, d\tau \\ &\quad = \int_\tau \int_\xi \int_\eta a_1 b_1 \, d\eta \, d\xi \, d\tau + ... + \int_\tau \int_\xi \int_\eta a_2 b_1 \, d\eta \, d\xi \, d\tau + ... + \int_\tau \int_\xi \int_\eta a_M b_N \, d\eta \, d\xi \, d\tau. \end{aligned} \tag{C.4}$$

Each integral in the expanded sum of Equation (C.4) is

$$\int_\tau \int_\xi \int_\eta a_m b_n \, d\eta \, d\xi \, d\tau = \int_\tau \int_\xi \int_\eta \big[X_{ma}(\xi) Y_{ma}(\eta) T_a(\tau) \big] \big[X_{nb}(\xi) Y_{nb}(\eta) T_b(\tau) \big] \, d\eta \, d\xi \, d\tau. \tag{C.5}$$

Due to the independence of $X(\xi)$, $Y(\eta)$ and $T(\tau)$ as well as the orthogonality of ξ, η and τ, Equation (C.5) becomes

$$\int_\tau \int_\xi \int_\eta a_m b_n \, d\eta \, d\xi \, d\tau = \left(\int_\xi X_{ma}(\xi) X_{nb}(\xi) \, d\xi \right) \left(\int_\eta Y_{ma}(\eta) Y_{nb}(\eta) \, d\eta \right) \left(\int_\tau T_a(\tau) T_b(\tau) \, d\tau \right). \tag{C.6}$$

Observing that $X_m(\xi) = \sin(m\pi\xi)$ for ψ, $\hat{\psi}_p$ and $\hat{\psi}_c$, leads to

$$\int_0^1 X_{ma}(\xi) X_{nb}(\xi) \, d\xi = \begin{cases} 1/2 & m = n \\ 0 & m \neq n \end{cases}. \tag{C.7}$$

Due to the orthogonality of the Fourier series, only terms where $m = n$ of the sum given by Equation (C.4) contribute. It becomes necessary to take either the real (or imaginary) term of the integrand to compute the norm. Because the the error terms introduced in Equation (2.7) are complex, the boundary function Fourier coefficients Γ_m become complex, leading to complex coefficients of Y_m. Given that $T(\tau) = e^{i\Omega\tau}$ leads to

$$\operatorname{Re}(Y_m e^{i\Omega\tau}) = \operatorname{Re}(Y_m)\cos(\Omega\tau) - \operatorname{Im}(Y_m)\sin(\Omega\tau). \tag{C.8}$$

The integral over τ and η becomes

$$\begin{aligned}
&\int_\tau \int_\eta \operatorname{Re}\left(Y_{ma}T\right) \operatorname{Re}\left(Y_{mb}T\right)\, d\eta\, d\tau = \\
&\int_\tau \int_\eta \operatorname{Re}(Y_{ma}) \operatorname{Re}(Y_{mb}) \cos^2(\Omega\tau)\, d\eta\, d\tau + \int_\tau \int_\eta \operatorname{Im}(Y_{ma}) \operatorname{Im}(Y_{mb}) \sin^2(\Omega\tau)\, d\eta\, d\tau, \\
-&\int_\tau \int_\eta \big(\operatorname{Re}(Y_{ma}) \operatorname{Im}(Y_{mb}) + \operatorname{Im}(Y_{ma}) \operatorname{Re}(Y_{mb})\big) \sin(\Omega\tau)\cos(\Omega\tau)\, d\eta\, d\tau.
\end{aligned} \tag{C.9}$$

Taking the time integral over one period, $\tau \in [0, \frac{2\pi}{\Omega}]$, and noting that $\operatorname{Im}\psi = 0$ and $\operatorname{Re}\psi = \psi$, leads to the following forms of Equation (3.45):

$$||e_{pw}||^2 = \frac{\pi}{2\Omega} \sum_{m=1,3,\ldots}^{M} \left(\int_0^{\eta_1} Y_m^2\, d\eta + \int_0^{\eta_1} \left(\operatorname{Re}(Y_{pm})^2 + \operatorname{Im}(Y_{pm})^2\right) d\eta - 2\int_0^{\eta_1} Y_m \operatorname{Re}(Y_{pm})\, d\eta \right), \tag{C.10a}$$

$$||e_{cw}||^2 = \frac{\pi}{2\Omega} \sum_{m=1,3,\ldots}^{M} \left(\int_{\eta_1}^{1} Y_m^2\, d\eta + \int_{\eta_1}^{1} \left(\operatorname{Re}(Y_{cm})^2 + \operatorname{Im}(Y_{cm})^2\right) d\eta - 2\int_{\eta_1}^{1} Y_m \operatorname{Re}(Y_{cm})\, d\eta \right). \tag{C.10b}$$

Appendix D

Real-Time Hybrid Simulation with Large Computational Substructures

Hybrid simulation to date has been primarily limited to framed structures involving computational substructures with relatively few degrees of freedom (DOFs). It has been noted that in real-time applications, which become important for rate-dependent response, not suitable for pseudodynamic tests [Nakashima 2001]; the presence of computational intensive analytical models may cause some significant issues [Mosalam and Günay 2013]. Because many of the problems of interest today such as soil-structure interaction, fluid dynamics, multi-physics simulations, etc., involve computational intensive numerical models, it is important to study the limitations of real-time hybrid simulation.

The tests performed were similar to that of Figure 1.1 at the micronees@berkeley experimental site [nees@berkeley 2013]. For a computational model, a framed structure was considered but varied in size such that more DOFs can be parametrically added and quantified by its computational intensity (i.e., bandwidth of the banded-matrix equations being solved [Strang 2005]). The computational driver used was Open System for Earthquake Engineering Simulation (OpenSEES) [OpenSEES 2013], and the model was subjected to a selected transient ground motion record, namely the 1940 El Centro ground acceleration record [Chopra 2004]. One of the ground-level columns is taken as the physical substructure in the laboratory. The intent of the simulations was not to model a particular problem but to study the effects of a large computational substructure. Material nonlinearity was subsequently added to the *computational* substructure.

Figure D.1 shows a comparison of "slower than real-time" and real-time hybrid simulation response with accepted pure simulation results. Significant errors are observed for real-time hybrid simulation. Figure D.2 shows a Fourier spectrum [Chopra 2004] of the response indicating an excitation at about 100 Hz, which is consistent with the hydraulic oil-column of the actuator in the test set-up [Mosqueda 2003]. Several mitigation strategies were proposed such as integration algorithms with numerical damping [Combescure and Pegon 1997] and a real-time filtering strategy, but these problem-specific solutions are typically not general in scope. For example, the addition of material nonlinearity as shown in Figure D.3 with the strategies proposed still shows an excitation in the Fourier spectrum consistent with the natural frequency of the physical column at about 20 Hz.

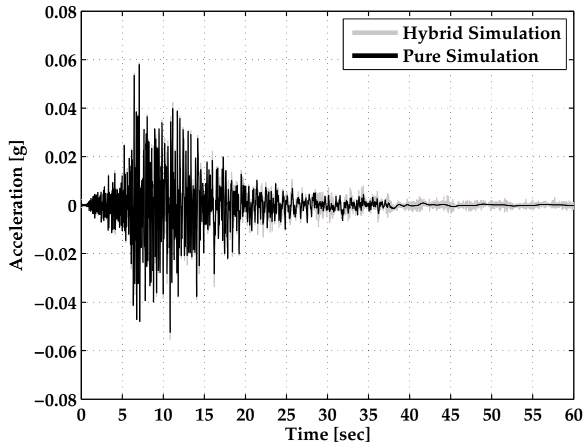

(a) Slower than real-time

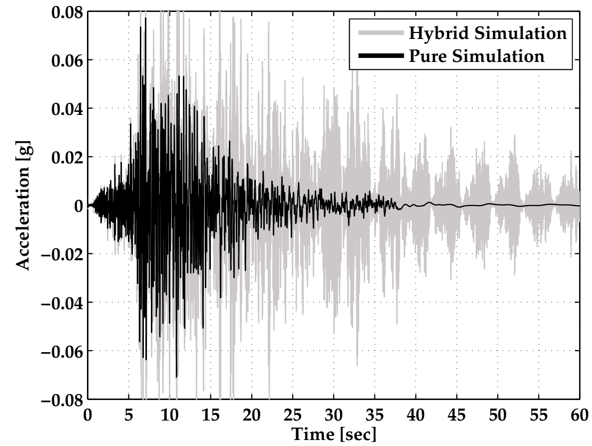

(b) Real-time

Figure D.1: Acceleration response history at the interface between the computational and physical substructures.

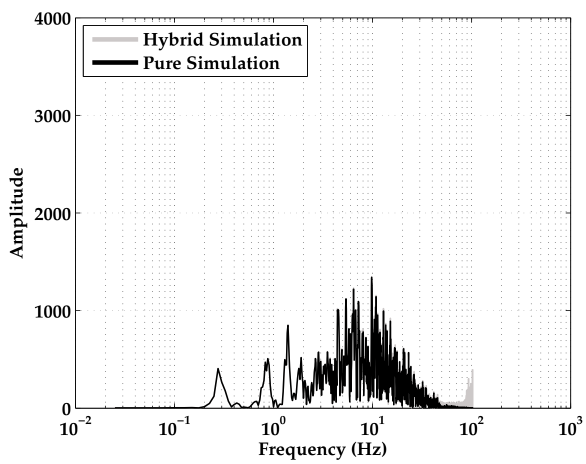

(a) Slower than real-time

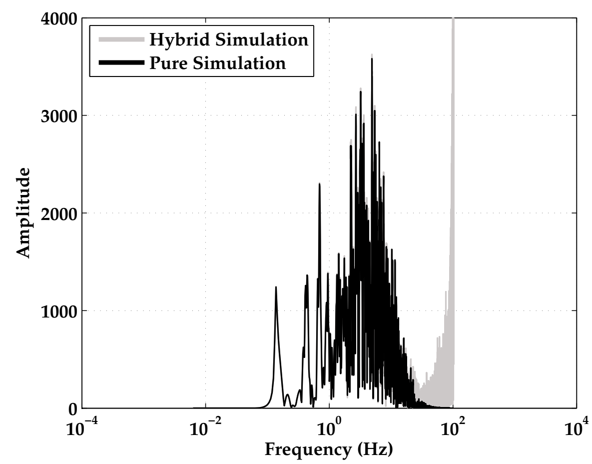

(b) Real-time

Figure D.2: Fourier spectrum of acceleration response history at the interface between the computational and physical substructures.

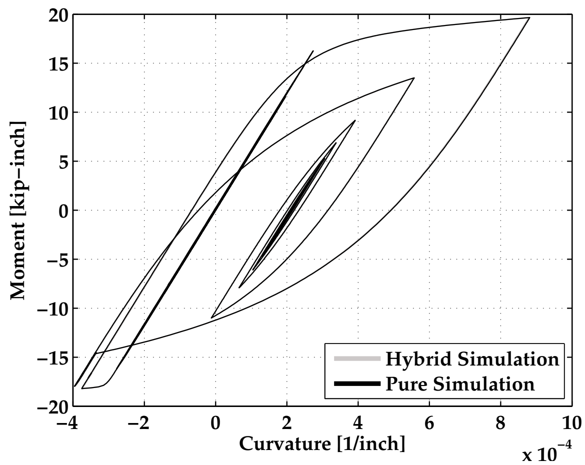

(a) Element force-deformation hysteresis

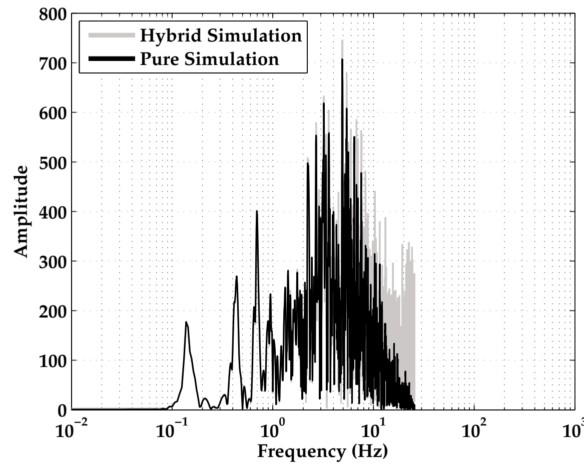

(b) Acceleration response Fourier spectrum

Figure D.3: Hybrid simulation with nonlinear material response of the computational substructure.

Finally, Figure D.4 shows a comparison of the measured force-displacement response to a purely numerical simulation at two different computational model sizes. As the computational intensity of the model grows past a certain point, the numerical equations being solved at each time step cannot keep up with the real-time control, and erroneous results are observed.

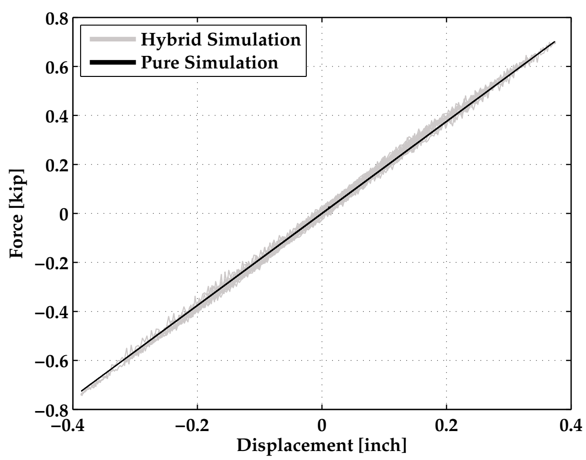

(a) 720 DOF

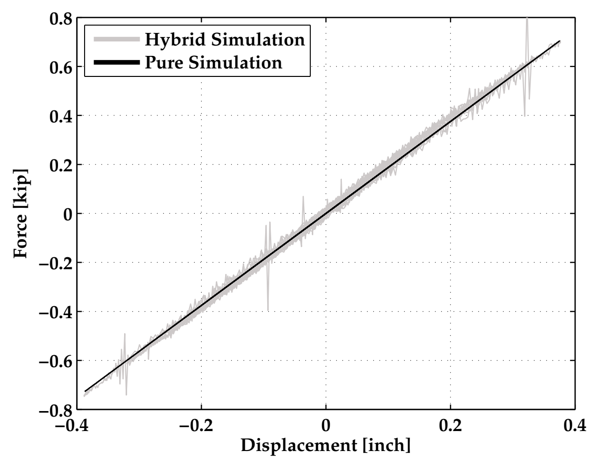

(b) 780 DOF

Figure D.4: Demonstration of computational limitations in real-time hybrid simulation.